A tectonic model for the juxtaposition of granulite- and amphibolite-facies rocks in the Eburnean orogenic belt (Sassandra-Cavally domain, Côte d'Ivoire)

Augustin Yao Koffi, Lenka Baratoux, Pavel Pitra, Alain Nicaise Kouamelan, Olivier Vanderhaeghe, Nicolas Thébaud, Olivier Bruguier, Sylvain Block, Hervé Jean-Luc Fossou Kouadio, Jacques Kone

BSGF - Earth Sciences Bulletin 2023, 194, 11
© A.Y. Koffi *et al.*, Published by EDP Sciences 2023
https://doi.org/10.1051/bsgf/2023007

BSGF Earth Sciences Bulletin
Available online at:
www.bsgf.fr

A tectonic model for the juxtaposition of granulite- and amphibolite-facies rocks in the Eburnean orogenic belt (Sassandra-Cavally domain, Côte d'Ivoire)

Augustin Yao Koffi[1,*], Lenka Baratoux[1,2], Pavel Pitra[3,4], Alain Nicaise Kouamelan[1], Olivier Vanderhaeghe[2], Nicolas Thébaud[5], Olivier Bruguier[6], Sylvain Block[2], Hervé Jean-Luc Fossou Kouadio[1] and Jacques Kone[2,7]

[1] UFHB Abidjan-Cocody, UFR STRM, 22 BP 582, Abidjan 22, Côte d'Ivoire
[2] GET, Université de Toulouse, CNRS, IRD, UPS, Toulouse, France
[3] Univ Rennes, CNRS, Géosciences Rennes, UMR 6118, 35000 Rennes, France
[4] Czech Geological Survey, Klárov 3, CZ-118 21, Praha 1, Czech Republic
[5] University Western Australia, School of Earth Sciences, Centre of Exploration Targeting, 35 Stirling Highway, 6009 Crawley, Australia
[6] Géosciences Montpellier, Université Montpellier – CNRS CC 060, Place Eugène Bataillon, 34095 Montpellier Cedex 5, France
[7] Department of Geology, Faculty of Science and Technology, Cheikh Anta Diop University, Dakar, Senegal

Received: 6 January 2023 / Accepted: 31 May 2023 / Publishing online: 4 August 2023

Abstract – The Sassandra-Cavally (SASCA) domain (SW Côte d'Ivoire) marks the transition between the Archean Kenema-Man craton and the Paleoproterozoic (Rhyacian) Baoule-Mossi domain. It is characterized by the tectonic juxtaposition of granulite-facies and amphibolite-facies rocks. Migmatitic grey gneisses, garnet–cordierite–sillimanite migmatitic paragneisses and garnet–staurolite-bearing micaschists reached peak pressure conditions ranging from ~6.6 kbar at 620 °C to ~10 kbar at 820 °C. These conditions are associated with the first recorded deformation D_1 and correspond to a Barrovian geothermal gradient of ~25 °C/km. Subsequent exhumation, associated with a second deformation D_2, was marked by decompression followed by cooling along apparent geothermal gradients of ~40 °C/km. A D_3 deformation phase is marked by folding and local transposition of the regional S_1/S_2 foliation into E-W trending shear zones. LA-ICP-MS U–Pb dating of monazite, which displays complex internal structures, reveals four age groups correlated to textural position of monazite grains and analytical points: (1) rare relictual zones yield dates at the Archean-Paleoproterozoic transition (ca. 2400–2600 Ma); (2) a cluster of dates centered at ca. 2037 Ma on grains aligned along the S_2 foliation of the migmatitic grey gneiss, attributed to D_2; (3) a cluster of dates centered at ca. 2000 Ma, and (4) dates spreading from ca. 1978 to 1913 Ma, documented for the first time in the West African Craton monazites. The ages of the latter two groups are similar to the ones identified in the Guiana Shield, and could be attributed to a disturbance by fluids, to a periodic opening of U–Pb system or to an episodic crystallization of monazite during slow cooling lasting several tens of Myrs. These data allow to propose a model for the tectonic evolution of the SASCA domain at the contact between the Rhyacian Baoule-Mossi domain and the Archean Kenema-Man nucleus whereby crustal thickening is achieved by crustal-scale folding and is followed by and concomitant with lateral flow of the thickened partially molten crust accommodated by regional transcurrent shear zones. This combination of crustal thickening controlled by tectonic forces and gravity-driven flow leads to the juxtaposition of granulite- and amphibolite-facies rocks.

Keywords: exhumation / Archean / Paleoproterozoic / monazite geochronology / West African Craton / Côte d'Ivoire

Résumé – Un modèle tectonique pour la juxtaposition de roches de faciès granulite et amphibolite dans la ceinture orogénique éburnéenne (domaine de Sassandra-Cavally, Côte d'Ivoire). Le domaine de Sassandra-Cavally (SASCA) (SW Côte d'Ivoire) marque la transition entre le craton archéen de Kenema-Man et le domaine paléoprotérozoïque (rhyacien) de Baoulé-Mossi. Il est caractérisé par la juxtaposition

*Corresponding author: yaoaugustinkoffi@yahoo.fr

tectonique de roches de faciès granulite et de faciès amphibolite. Les gneiss gris migmatitiques, les paragneiss migmatitiques à grenat–cordiérite–sillimanite et les micaschistes à grenat–staurotide ont atteint des conditions de pression maximale allant de ~ 6,6 kbar à 620 °C à ~ 10 kbar à 820 °C. Ces conditions sont associées à la première déformation enregistrée D_1 et correspondent à un gradient géothermique barrovien de ~ 25 °C/km. L'exhumation ultérieure, associée à une deuxième déformation D_2 a été marquée par une décompression suivie d'un refroidissement le long de gradients géothermiques apparents de ~ 40 °C/km. Une phase de déformation D_3 est marquée par un plissement et une transposition locale de la foliation régionale S_1/S_2 en zones de cisaillement orientées E-W. La datation U–Pb par LA-ICP-MS de la monazite qui présente des structures internes complexes révèle quatre groupes d'âge corrélés à la position texturale des grains de monazite et aux points d'analyse : (1) de rares zones relictuelles donnent des âges à la transition Archéen-Paléoprotérozoïque (ca. 2400–2600 Ma) ; (2) un groupe d'âges à environ 2037 Ma sur des cristaux alignés le long de la foliation S_2 du gneiss gris migmatitique, attribué à D_2 ; (3) un groupe d'âges à environ 2000 Ma, et (4) des âges s'étalant d'environ 1978 à 1913 Ma documentés pour la première fois dans les monazites du Craton ouest-africain. Les âges de ces deux derniers groupes sont similaires à ceux identifiés dans le Bouclier guyanais, et pourraient être attribués à une perturbation par des fluides, à une ouverture périodique du système U–Pb ou à une cristallisation épisodique de la monazite lors d'un refroidissement lent de plusieurs dizaines de millions d'années. Ces données permettent de proposer un modèle pour l'évolution tectonique du domaine SASCA au contact entre les domaines rhyaciens de Baoule-Mossi et le noyau archéen de Kenema-Man dans lequel l'épaississement crustal est réalisé par un plissement à l'échelle crustale et est suivi et concomitant d'un écoulement latéral de la croûte épaissie partiellement fondue accommodée par des zones de cisaillement régionales transcurrentes. Cette combinaison d'épaississement crustal contrôlé par des forces tectoniques et d'écoulement par gravité conduit à la juxtaposition de roches de faciès granulite et amphibolite.

Mots clés : exhumation / Archéen / Paléoprotérozoïque / géochronologie de la monazite / Craton Ouest-Africain / Côte d'Ivoire

1 Introduction

Tectonic regimes on Earth have undergone a secular change in style mainly due to the cooling of the planet during the Archean-Paleoproterozoic period (3.0–2.0 Ga). The tectonic processes operating on Early Earth are vividly debated in the literature and it remains an open question when plate tectonic processes such as Earth-wide subduction and orogenesis began (Kranendonk, 2010; Condie, 2018; Palin *et al.*, 2020; Brown *et al.*, 2020). Many authors place the transition from the so-called "stagnant-lid" to some kind of plate tectonics in the Meso-Archean period (Cawood *et al.*, 2013; Palin *et al.*, 2020) but some propose that it occurred early in the Earth's history, at ca. 4 Ga (Maruyama *et al.*, 2018) or, much later, at ca. 1 Ga (Stern, 2005; Hamilton, 2011). The nature of the transition from stagnant-lid to mobile-lid tectonics is also questioned (Palin *et al.*, 2020), in particular whether the crustal record is representative of lithospheric scale processes or of crustal dynamics (Vanderhaeghe *et al.*, 2019).

The Paleoproterozoic Eburnean orogeny (2.25–1.9 Ga) in the West African Craton (WAC) exemplifies this controversy. Some authors advocate an "archaic", "hot-lithosphere" style dominated by vertical movements and the emplacement of granitic plutons separated by greenstone belts (Condie, 1994; de Wit, 1998; Gapais *et al.*, 2005, 2008; Bédard, 2006; Vidal *et al.*, 2009). Others argue that Paleoproterozoic tectonics shares many similarities with "modern", "cold-lithosphere" plate tectonics characterized by tangential movements leading to crustal thickening and magmatism (Feybesse and Milési, 1994; Ledru *et al.*, 1994). A critical point for the understanding of the tectonic regime prevailing during the Paleoproterozoic Eburnean orogeny in the WAC is the lack of data on the metamorphic conditions, their evolution, and relative and absolute timing. Metamorphic petrology combined with geochronology provides a record of the secular cooling of the Earth in Archean and Paleoproterozoic domains exposing dominantly high-temperature metamorphic rocks (Brown, 2014). The coexistence of high-pressure eclogite- to granulite-facies metamorphism recording gradients of 15 to 25 °C/km and (ultra) high-temperature granulite-facies metamorphism with gradients of 30 to 40 °C/km in Paleoproterozoic belts appears to characterize the so-called "modern" geodynamic context (Brown, 2014).

The genesis of high-pressure (HP) metamorphic rocks in Archean and Paleoproterozoic domains and the mechanisms leading to their exhumation are debated in different parts of the WAC (western Côte d'Ivoire: Pitra *et al.*, 2010; eastern Burkina Faso: Ganne *et al.*, 2012; NW Ghana: Block *et al.*, 2015; SW Ghana: McFarlane *et al.*, 2019). In the Kouibli zone in the West of Côte d'Ivoire, maximum metamorphic conditions preserved at the contact zone between the Archean and Paleoproterozoic domains are in the granulite facies ranging from ~ 14 kbar, 850 °C to ~ 7 kbar, 700–800 °C (Triboulet and Feybesse, 1998; Pitra *et al.*, 2010) and dated between 2050 and 2030 Ma (Th–U–total Pb monazite microprobe ages: Cocherie *et al.*, 1998; Sm–Nd garnet ages: Kouamelan *et al.*, 1997). Archean ages ranging from ca. 2800 to 2700 Ma were documented in monazite cores from the same samples by both evaporation and microprobe Th–U–Pb methods (Cocherie *et al.*, 1998).

The Sassandra-Cavally (SASCA) domain (named after the two rivers that run across the area) represents a contact zone between the Archean and Paleoproterozoic domains of the West African Craton in the SW Côte d'Ivoire (Kouamelan, 1996; Kouamelan *et al.*, 1997, 2015). Neither P–T estimations

nor metamorphic ages exist in the SASCA domain where the last mapping was done by Papon (1973). The only LA-ICP-MS U–Pb zircon ages are from San Pedro tonalitic gneiss (SA-3) and yield ages of 3207 ± 7 Ma for magmatic zircon grains and an upper intercept of 3155 ± 17 Ma on some magmatic zircon rims and rounded grains (Kouamelan *et al.*, 2015). Younger ages were not found in the studied sample, leading the authors to a conclusion that the gneiss was unaffected by the Eburnean orogeny.

In order to decipher the P–T conditions and timing of deformation of the SASCA domain, we apply a multimethod approach combining field geology, (micro)structural analysis, metamorphic petrology and LA-ICP-MS U–Pb geochronology on monazite. These data are used to discuss the thermal and tectonic regime and timing of the Eburnean reworking of the Archean crust.

2 Geological setting of the West African Craton

Precambrian domain in the West African Craton crop out in four regions of unequal sizes: the Reguibat Shield in the North, the Leo-Man Shield in the South (Berger *et al.*, 2013; Jessell *et al.*, 2015; Thiéblemont, 2016) and the significantly smaller Paleoproterozoic Kédougou-Kéniéba and Kayes inliers between the two shields (Ledru *et al.*, 1991; Kone *et al.*, 2020; Labou *et al.*, 2020; Diallo *et al.*, 2021) (Fig. 1). The Leo-Man and Reguibat Shields consist of Paleoproterozoic formations in the East and Archean formations in the West separated by transcurrent shear zones (Bessoles, 1977; Camil, 1984; Auvray *et al.*, 1992; Kouamelan, 1996; Potrel *et al.*, 1996; Kouamelan *et al.*, 1997; Thiéblemont *et al.*, 2001, 2004; Peucat *et al.*, 2005; Pitra *et al.*, 2010). Three major orogenic episodes mark the history of the WAC: the Leonian (3.4–3.0 Ga), the Liberian (2.9–2.7 Ga) and the Eburnean (2.25–1.9 Ga) after which the whole craton was stabilized (Thiéblemont *et al.*, 2004; Liégeois *et al.*, 2005; Begg *et al.*, 2009; De Waele *et al.*, 2015; Wane *et al.*, 2018). In the Leo-Man Shield, the Archean domain is called Kenema-Man while the Paleoproterozoic domain to the east is known as the Baoule-Mossi domain (Bessoles, 1977). The Archean Kenema-Man domain consists of two main complexes: a basal complex consisting of migmatites and granulitic gneisses unconformably overlain by a sequence of supracrustal rocks deformed and metamorphosed at 2800 ± 20 Ma (Camil, 1981, 1984; Rollinson and Cliff, 1982; Martin, 1994; Kouamelan, 1996; Rollinson, 2016). The basal complex is intruded by various plutonic rocks including granite, granodiorite, charnockite, as well as basic and ultrabasic rocks dated around 2.8 Ga (Rollinson and Cliff, 1982; Kouamelan *et al.*, 1997; Thiéblemont *et al.*, 2001; Rollinson, 2016). The supracrustal rocks reached medium- to high-pressure granulite facies during the Liberian (~ 2700 Ma) orogeny (Williams, 1988).

The Paleoproterozoic Baoule-Mossi domain consists of belts of metavolcanic (metarhyolite, metadacite, metaandesite, metabasalt, etc.) and metasedimentary (metapelite, metasandstone, metaconglomerate, quartzite etc.) rocks juxtaposed to granitoid batholiths (Leube *et al.*, 1990; Doumbia *et al.*, 1998; Gasquet *et al.*, 2003; Pouclet *et al.*, 2006; Lompo, 2009; Baratoux *et al.*, 2011). The emplacement and the subsequent reworking of all these lithologies occurred from ca. 2.25 to 2.06 Ga (Parra-Avila *et al.*, 2017). The structural grain of the Baoule-Mossi domain is characterized by a subvertical penetrative foliation, associated with isoclinal folds and locally affected by more open folds and by regional-scale shear zones. This structural framework is interpreted by many authors as a result of horizontal shortening leading to crustal thickening followed by transcurrent tectonics (Lemoine *et al.*, 1985; Lemoine, 1988; Milési *et al.*, 1989, 1992; Feybesse *et al.*, 1990, 2006; Ledru *et al.*, 1991; Boher *et al.*, 1992; Fabre, 1995; Vidal *et al.*, 1996, 2009; Bourges *et al.*, 1998; Allibone *et al.*, 2002; Lompo, 2010; Baratoux *et al.*, 2011; Jessell *et al.*, 2012; Block *et al.*, 2016). Some works suggest an "archaic" style of deformation for the Baoule-Mossi domain, dominated by gravity-driven vertical motions in a hotter lithosphere compared to post-Paleoproterozoic period (Delor *et al.*, 1995; Pouclet *et al.*, 1996; Vidal *et al.*, 1996, 2009; Caby *et al.*, 2000). The "archaic" style is characterized by the development of "dome and basin" structures with isobaric metamorphism in the contact aureoles of the granitoids attributed to the development of gravitational instabilities caused by the presence of dense supracrustal mafic volcanic rocks over buoyant granitoid domains (Pons *et al.*, 1995; Pouclet *et al.*, 1996; Caby *et al.*, 2000; Vidal *et al.*, 2009; Lompo, 2010; Ganne *et al.*, 2014). In this model, upwelling of migmatitic rocks to the surface is buoyancy-driven in a hot and rheologically weak orogenic crust and is associated with crustal thickening (Caby *et al.*, 2000; Ganne *et al.*, 2014). As an alternative model, Chardon *et al.* (2020) interpret the craton-scale shear zone pattern as a result of distributed shortening and lateral flow of the hot lithosphere leading to an anastomosed transpressional shear zone network. The Eburnean orogeny is also marked by partial melting and melt segregation, which leads to the petrogenesis of a variety of pegmatites, some of which are enriched in REE (Bonzi *et al.*, 2021).

Based on the cold apparent geothermal gradients in the volcano-sedimentary rocks from Burkina Faso, Ganne *et al.* (2012) suggested that the Eburnean orogenic belt in the Baoule-Mossi domain formed owing to modern-style tectonics marked by subduction. In the Baoule-Mossi domain, greenschist-facies conditions are predominant in the greenstone belts. However, recent work of Block *et al.* (2015) and McFarlane (2018) have shown large domains of Barrovian-type high-grade metamorphism attributed to continental collision with the peak of metamorphism spanning between 2138 ± 7 Ma and 2127 ± 7 Ma (Block *et al.*, 2015) and 2073 ± 2 Ma (McFarlane *et al.*, 2019) (U–Pb on monazite). In addition, migmatites were reported by Opare-Addo *et al.* (1993) from southern Ghana. At other places, amphibolite-facies metamorphism is interpreted as contact metamorphism around magmatic intrusions at 1973 ± 33 Ma (Ndiaye *et al.*, 1989; Debat *et al.*, 2003). Medium- to high-pressure granulite-facies rocks characterize the boundary zone between the Archean and Paleoproterozoic domains in the Côte d'Ivoire (Triboulet and Feybesse, 1998; Caby *et al.*, 2000; Pitra *et al.*, 2010) and suggest a Paleoproterozoic granulite-facies metamorphic overprint at 2053 ± 15 Ma and 2031 ± 13 Ma (Sm–Nd garnet, Kouamelan *et al.*, 1997; Pitra *et al.*, 2010). Also, Paleoproterozoic ages of 2041 ± 19 Ma and 2037 ± 14 Ma were obtained in high-grade metamorphic rocks in southeastern

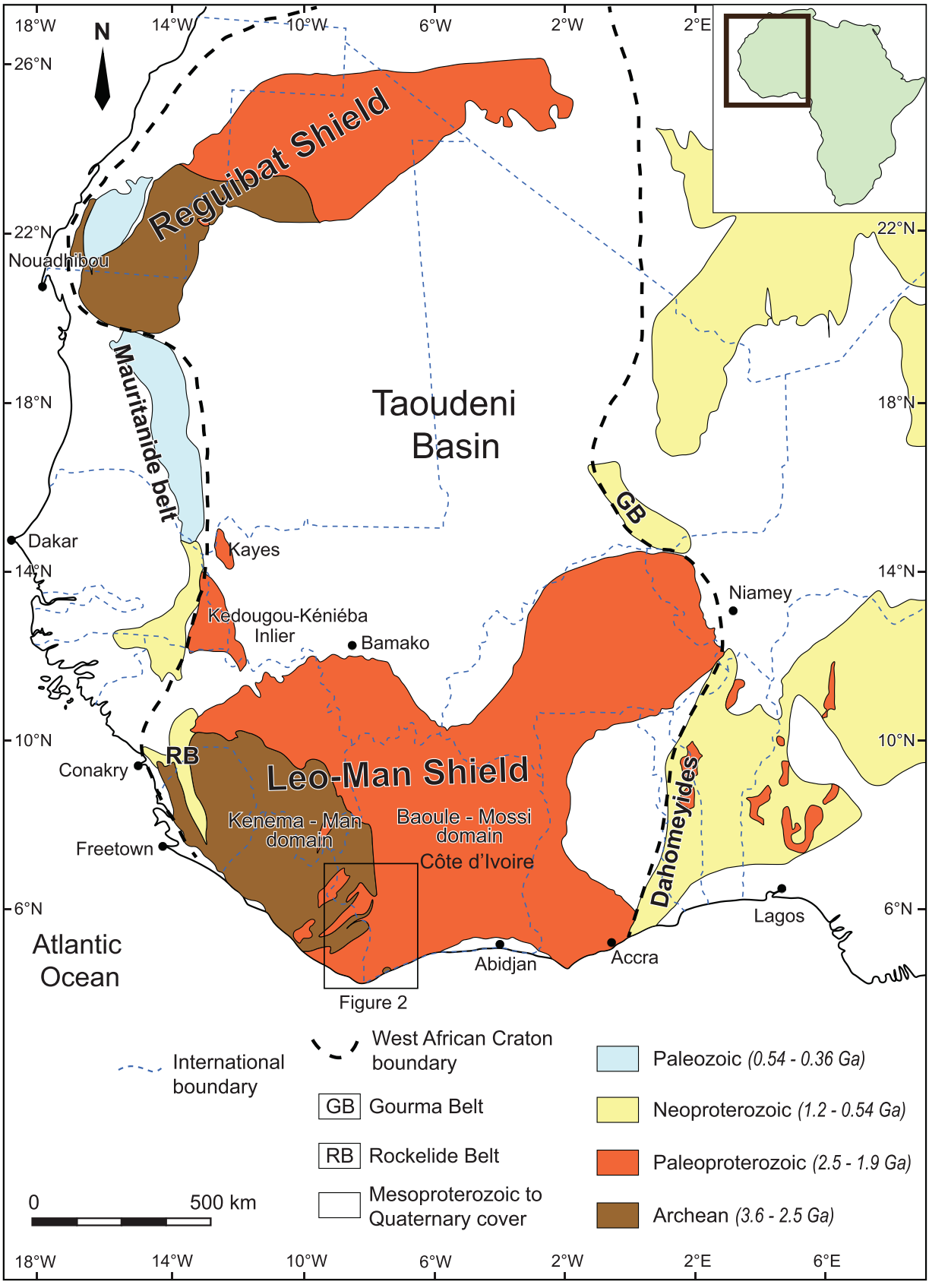

Fig. 1. Geological sketch map of the West African Craton (modified after the BRGM SIG Africa map and Ennih and Liégeois, 2008; Berger *et al.*, 2013; Thiéblemont, 2016). The position of the present-day margins of the craton is constrained by geophysics (Jessell *et al.*, 2015).

Guinea (U–Pb SHRIMP on zircon; Thiéblemont *et al.*, 2004). The ages obtained in the Damang gold deposit (Ghana) suggest a timing of mineralization around 2005 ± 26 Ma (U–Th–Pb EMPA on monazite). The cooling ages obtained by the $^{40}Ar/^{39}Ar$ method on biotite range from 1980 ± 9 to 1898 ± 11 Ma (White *et al.*, 2014).

In the Kedougou-Kéniéba Inlier, U–Pb monazite metamorphic ages from the Saraya batholith in Senegal yield 2064 ± 4 Ma (Hirdes and Davis, 2002) and a maximum age for the deposition of the sedimentary protolith of the Dialé-Daléma series is given by U–Pb on detrital zircon grains at 2120–2110 Ma (Kone *et al.*, 2020).

3 Geology of the SASCA domain

The SASCA domain is mainly built of migmatitic grey gneisses commonly intercalated with amphibolites and metasediments, also locally migmatitic (Fig. 2). Metasedimentary rocks occur as staurolite-bearing micaschists and banded paragneisses. In the southernmost part (region of Tabou; Fig. 2), diopside- and hypersthene-bearing metabasic granulitic gneisses predominate. These lithological units are intruded by granites, granodiorites, syenites, as well as associated aplites and pegmatites (Papon, 1973), and crosscut by large ductile structures such as the Greenville-Ferkessédougou-Bobo-Dioulasso shear zone (Lemoine *et al.*, 1985; Baratoux *et al.*, 2011).

Geochronological data on the migmatitic grey gneisses of San Pedro and Monogaga (samples SP3B, SP11 and MON4 in Fig. 2) revealed the presence of Archean crustal relics, with a majority of zircon U–Pb ages ranging from ca. 2800 to 3330 Ma (monozircon evaporation: Kouamelan *et al.*, 1997; LA-ICP-MS: Kouamelan *et al.*, 2015; LA-(MC)-ICP-MS: Koffi *et al.*, 2022). Sm–Nd model age of the magmatic protoliths of the migmatitic grey gneiss in the SASCA is 3.46 Ga (Sample SA-3, Kouamelan, 1996; Kouamelan *et al.*, 1997) and ε_{Hf} ranges from −9.4 to +3.3 (Koffi *et al.*, 2022). A potassic granite intrusion at San Pedro (sample CIS62 in Fig. 2) was dated at 2084 ± 6 Ma and yields a hybrid ε_{Hf} isotopic signature with clusters between −4.9 and −8.5, and between +2.2 and +6.5 for inherited zircon grains dated between ca. 2343 to 2100 Ma (Koffi *et al.*, 2022). The presence of Archean relics, negative ε_{Nd} values at 2.1 Ga in the migmatitic grey gneiss, and negative ε_{Hf} in the San Pedro potassic granite indicate some interaction between the Archean crust and the juvenile magmas formed during the Eburnean orogeny (Kouamelan *et al.*, 1997; Koffi *et al.*, 2022). The age of 2076 ± 6 Ma obtained on zircon rims from migmatitic gneiss from Monogaga (sample SP11 in Fig. 2) was interpreted as reflecting a metamorphic event. A garnet–cordierite–sillimanite migmatitic paragneiss from Grand-Béréby, deposited after 2069 ± 4 Ma (Koffi *et al.*, 2022), shows Sm–Nd model ages of 2.48 and 2.47 Ga confirming the Archean age of the source of the sedimentary protoliths (samples GDB8, KOU7) (Kouadio, 2017; Koffi *et al.*, 2022).

4 Methodology

4.1 Petrology

The chemical composition of minerals was determined using a CAMECA SXFive electron microprobe (Raimond Castaing Microcaracterization Center, Toulouse). The analytical conditions were 15 keV, 10 nA for biotite, chlorite, cordierite, white micas and staurolite, 20 nA for garnet and feldspar, and beam spot size < 2 μm. The acquisition times were 10 s on the peak and 5 s on either side of the peak for the continuous background.

P–T conditions were estimated using equilibrium assemblage phase diagrams (pseudosections) calculated in the chemical model system (Mn)NCKFMASHTO with the software Theriak/Domino (de Capitani and Brown, 1987; de Capitani and Petrakakis, 2010) and the internally consistent thermodynamic data set 5.5 (Holland and Powell, 2003). The full system including Mn is useful for examining lower-grade metamorphic conditions, as garnet is significantly stabilized by Mn to lower temperatures (Mahar *et al.*, 1997). Mineral abbreviations follow Holland and Powell (1998). The solution phases considered, and the mixing models used are from Holland and Powell (1998) – chloritoid (ctd), cordierite (cd), epidote (ep), staurolite (st); Holland and Powell (2003) – plagioclase (pl), K-feldspar (ksp); White *et al.* (2007) – garnet (g), biotite (bi), liquid (liq); Mahar *et al.* (1997) – chlorite (chl); Coggon and Holland (2002) – muscovite (mu), paragonite (pa); White *et al.* (2000) – ilmenite (ilm), hematite (hem) and White and Powell (2002) – magnetite (mt), orthopyroxene (opx). Albite (ab), andalusite (and), kyanite (ky), quartz (q), rutile (ru), sillimanite (sill) and titanite (sphene, sph) are considered as pure end members. Bulk rock compositions of the samples were measured from rock powders at Bureau Veritas Commodities Canada Ltd by ICP-AES (Tabs. 1 and 2). The amount of Fe^{3+} (with respect to total Fe) was estimated using calculated P/T-X(Fe^{3+}) pseudosections and the nature of the oxide (ilmenite, magnetite or hematite) observed in the samples. At temperatures below the solidus, all pseudosections were calculated considering H_2O in excess. The amount of H_2O for calculating liquid (melt) bearing equilibria was fixed so that the mineral assemblages are just H_2O-saturated (*i.e.*, contain a minimal amount, of the order of 1 vol%, of free aqueous fluid) below the solidus. Mineral endmembers (expressed in mole %) and compositional variables (molar ratios) are: $X_{Mg} = Mg/(Mg + Fe)$, $X_{Na} = Na/(Na + Ca + K)$, almandine, $Alm = Fe/(Fe + Mg + Ca + Mn)$, pyrope, $Prp = Mg/(Fe + Mg + Ca + Mn)$, grossular, $Grs = Ca/(Fe + Mg + Ca + Mn)$, spessartine, $Sps = Mn/(Fe + Mg + Ca + Mn)$, anorthite, $An = Ca/(Ca + Na + K)$; a.p.f.u. = atoms per formula unit; "→" denotes core-to-rim evolution.

4.2 Geochronology

The internal structure of the monazite crystals was characterized by a JEOL JSM 6360 LV microscope equipped with an X-ray detector connected to an EDS (Energy Dispersive Spectrometry) microanalyzer platform at the Laboratory of Environmental Geosciences Toulouse (GET) in France. All monazite crystals were scanned in BSE (Backscattered electron). LA-ICP-MS *in situ* U–Pb analyses of monazite were carried out directly on the thin sections at Geosciences Montpellier (France). The laser system consists of a Lambda Physik Compex 102 excimer laser coupled to a Thermofinnigan Element XR ICP-MS (AETE-ISO regional facility of the OSU OREME, University of Montpellier).

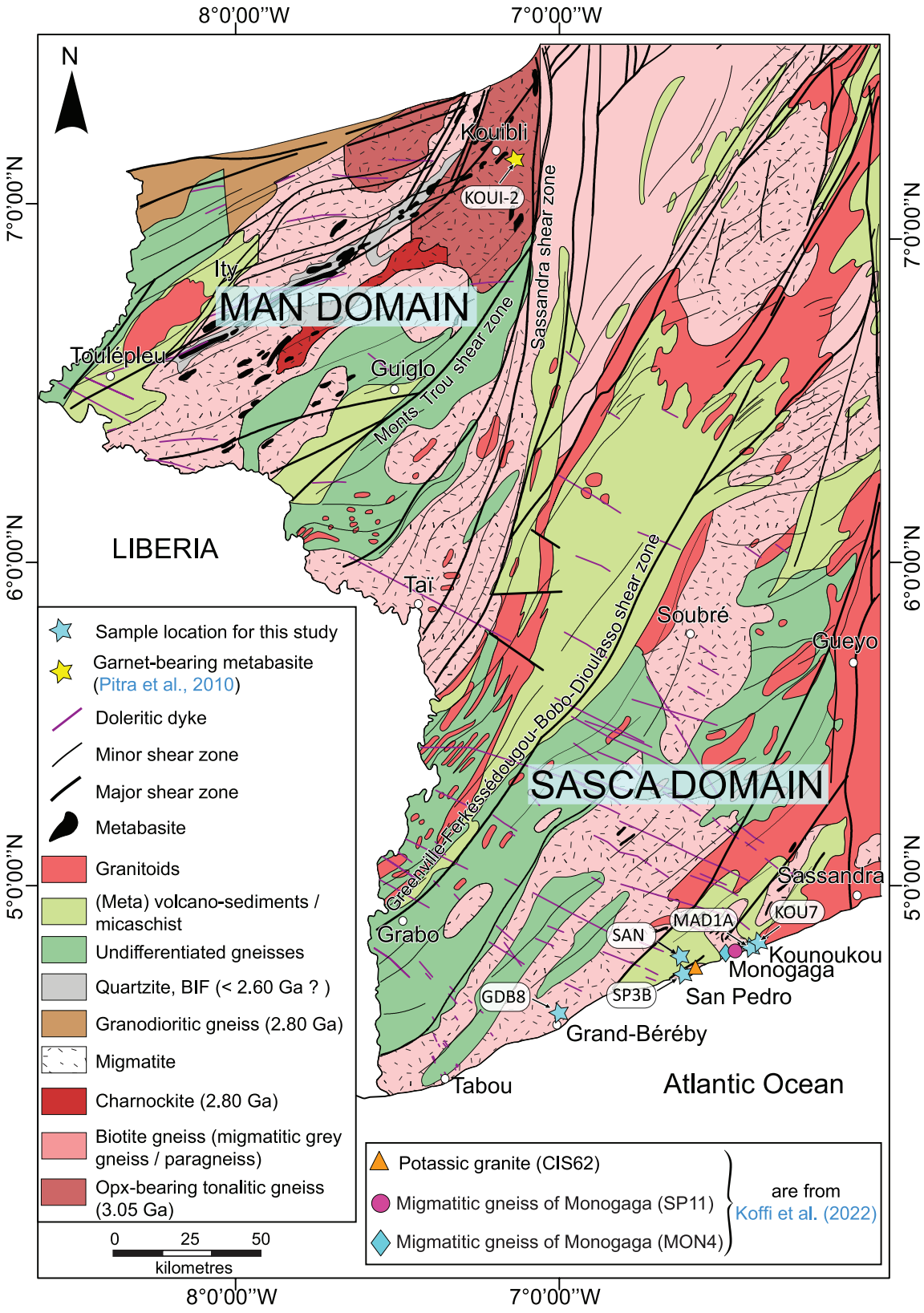

Fig. 2. Litho-structural map of the SW of Côte d'Ivoire (modified after Tagini, 1971; Papon, 1973; Pitra *et al.*, 2010; WAXI report, AMIRA Global, 2018). Blue stars show the location of the studied samples. Samples are described from West to East.

Table 1. Petrographic summary and location in degree (WGS 84 coordinate system) of the samples studied. Quartz, plagioclase, biotite and ilmenite are present in all samples.

Sample	Latitude	Longitude	Lithology	Dominant metamorphic assemblage
GDB8	4.7212280	−6.9533400	Garnet–cordierite–sillimanite migmatitic paragneiss	**g–cd–sill–liq**
SP3B	4.7229500	−6.6394600	Migmatitic grey gneiss	**g–liq**
SAN	4.7835400	−6.6472500	Staurolite-bearing micaschist	**st–and–chl–mt**
MAD1A	4.8127300	−6.4308700	Garnet–sillimanite–cordierite micaschist	**g–sill–cd**
KOU7	4.8216300	−6.3977500	Garnet–staurolite-bearing micaschist	**g–st**

Table 2. Chemical compositions (oxide wt%) of the samples used for the P–T pseudosection calculations. Fe_2O_3 corresponds to total Fe.

	wt%									
Sample	SiO_2	Al_2O_3	Fe_2O_3	MnO	MgO	CaO	Na_2O	K_2O	TiO_2	Total
SP3B	67.20	15.7	5.19	0.08	2.09	3.53	3.66	1.85	0.57	99.87
GDB8	56.40	19.60	10.40	0.12	3.92	1.97	3.19	2.20	0.99	98.79
SAN	56.00	24.10	9.25	0.10	3.45	0.69	1.34	2.37	0.88	98.18
MAD1A	66.10	16.10	6.25	0.02	2.94	1.83	1.74	2.00	0.63	97.61
KOU7	63.00	17.90	8.16	0.07	2.73	1.88	2.41	2.09	0.69	98.93

The instrument was tuned for maximum sensitivity and low oxide production (ThO/Th < 1%). Analytical conditions are identical to those reported in previous studies (*e.g.*, Bruguier *et al.*, 2009; Bosch *et al.*, 2011) where ablation experiments were performed under helium, which enhances sensitivity and reduces inter-element fractionation (Günther and Heinrich, 1999). The helium stream and particles ablated from the sample were mixed with Ar before entering the plasma. Laser spot size was 5 μm for monazite and the laser was operated at a repetition rate of 2 Hz using a 12 J/cm^2 energy density. Total analysis time was 60 s with the first 15 s used for background measurement, which was subtracted from the sample signal. Before each analysis the surface of the targeted zone was cleaned with 10 pulses using a spot size larger than the size used for U–Pb analysis. Pb/U and Pb/Pb ratios were calibrated against the Manangotry crystal (Poitrasson *et al.*, 2000). This reference material was used to correct the measured ratios for mass discrimination and inter-element fractionation. In the course of this study the Manangotry crystal was measured twice each five unknowns. The 57 analyses yielded a $^{207}Pb/^{206}Pb$ weighted average of 0.05866 ± 0.00015 (2σ) which corresponds to an age of 555 ± 6 Ma, in good agreement with the reference age for this material (Montel *et al.*, 1996; Horstwood *et al.*, 2003). U–Th–Pb isotopic data were reduced using the Glitter software (Van Achterbergh *et al.*, 2001) and ages were calculated using Isoplot (Ludwig, 2003) and are quoted in the text at the 2σ confidence level. Data points are considered concordant when their concordance degree is equal or higher than 95% (based on the comparison between the $^{206}Pb/^{238}U$ and $^{207}Pb/^{206}Pb$ apparent ages). For these analyses, a $^{207}Pb/^{206}Pb$ weighted mean age was favored. On the contrary, when data points are discordant (concordance < 95%), discordia lines were calculated (Fig. 3).

High spatial resolution mapping at 15 keV and 20 nA for 5–10 s per pixel on the CAMECA SXFive electron microprobe of Archean grey gneisses monazites (SP3B) larger than 100 μm was performed at a resolution of ca. 200 × 120 pixels per grain to visualize their complex chemical zonations. Chemical maps of Ce, Pb, Th, U, and Y were used to guide subsequent quantitative U–Pb analyses by LA-ICP-MS. The monazite data are summarized in Supplementary Materials (Tables S1, S2 and S3).

5 Results

5.1 Structural evolution

Based on the study of the coastal section between Grand-Béréby and Sassandra, three main phases of deformation (D_1–D_3) are documented in the SASCA region. The first phase D_1 is characterized by a NW-SE oriented S_1 subvertical penetrative metamorphic foliations in an axial planar position of tight isoclinal folds. The second phase of deformation D_2 is marked throughout the studied area by tight to open F_2 folds with subvertical NNE-SSW-trending axial planes parallel to the S_2 foliation and sinistral ductile shear zones. The L_2 lineation is parallel to the fold axes and plunges between 80° and 30° to the NNE. D_2 is interpreted as recording continuous NNW-SSE shortening under a transpressive regime. In the San Pedro area, D_1 and D_2 structures are overprinted by the deformation phase D_3 that is expressed as F_3 folds and a penetrative subvertical E-W axial planar schistosity S_3 associated with E-W-striking dextral shear zones suggesting a WNW-ESE shortening (Fig. 4). Geological cross-section and equal-area, lower hemisphere stereoplots document the structures related to the D_2 deformation phase (Figs. 4b and 4c, respectively). The relationship between structural observations and mineral assemblage will be discussed in the petrography and mineral chemistry section.

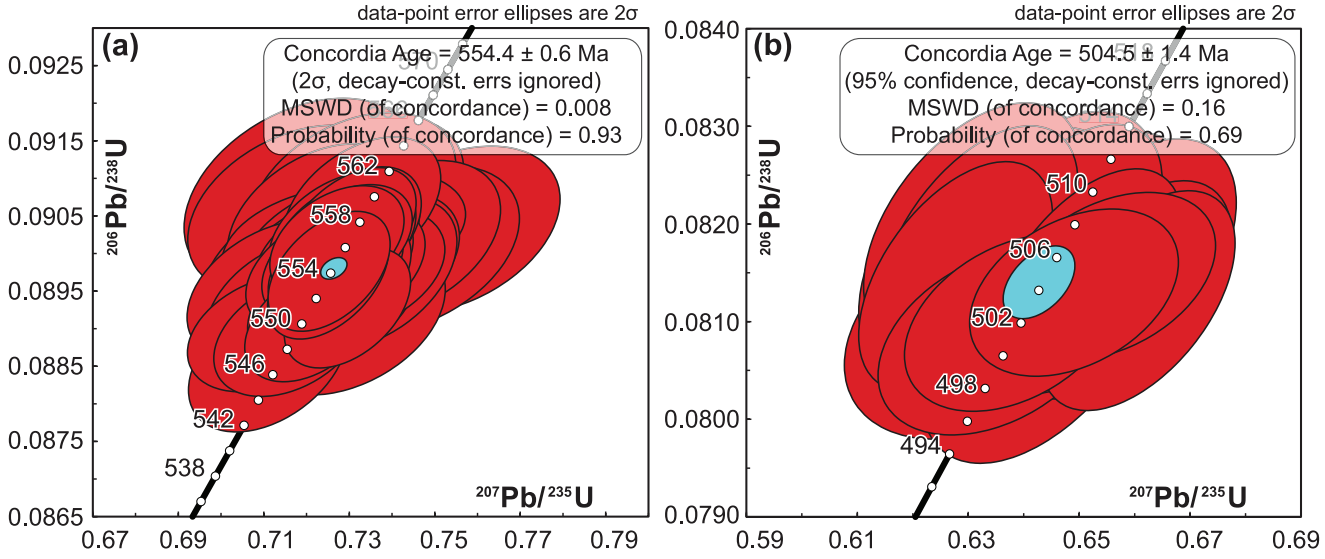

Fig. 3. Concordia plots of U–Pb age dating for reference material Manangotry and Moacyr monazites (a and b respectively).

5.2 Petrography and mineral chemistry

Five samples representative of the different lithological units of the SASCA domain were studied in detail (location and description in Figs. 2 and 5 and Tab. 1). Representative mineral compositions are reported in Tables 3a and 3b.

5.2.1 Garnet–cordierite–sillimanite migmatitic paragneiss (GDB8)

Macroscopically, the rock displays a prominent migmatitic layering S_1 folded by tight to open folds F_2 with ca. 30° NE-plunging fold axes and subvertical axial planes, parallel to a less penetrative foliation S_2. Coarse-grained quartzo-feldspathic leucosome layers (1–10 cm thick), rimmed by thin layers of biotite-rich melanosome, and alternating with layers of gneissic mesosome define the synmigmatitic foliation S_1 (Fig. 5a). The mesosome contains quartz, plagioclase (An23–25), biotite, euhedral prismatic sillimanite (long up to 0.5 mm), cordierite and ilmenite (Fig. 6a). Biotite and sillimanite define the foliation S_2 that wraps around anhedral porphyroblasts of garnet (up to 2.5 mm) and locally biotite that preserve S_1 inclusion trails. In garnet, S_1 is marked by abundant inclusions of fine needles of sillimanite (Fig. 6a). Garnet is commonly surrounded by cordierite (X_{Mg} = 0.79–0.85, Na up to 0.02 a.p.f.u.) and locally by symplectitic intergrowths of biotite and quartz. Garnet is chemically zoned with a rimward decrease of pyrope and X_{Mg}, and an increase of almandine and spessartine (Alm58→70 Prp34→23 Grs2-3 Sps4→5, X_{Mg} = 0.37→0.26; Fig. 7a). Biotite in the matrix and inclusions in cordierite have a constant X_{Mg} of ca. 0.60. Inclusions in garnet show a variable X_{Mg} (0.62–0.78). All biotite crystals contain 0.23–0.28 a.p.f.u. of Ti and up to 0.22 a.p.f.u. of F.

The inferred peak mineral assemblage comprises garnet, biotite, sillimanite, plagioclase, quartz, ilmenite, and melt. The significantly smaller size of sillimanite inclusions in garnet with respect to the matrix crystals testifies to a prograde growth of garnet, contemporaneous with S_1. Garnet zoning is attributed to diffusional reequilibration during partial resorption. Biotite-plagioclase symplectites around garnet suggest that the resorption may reflect reaction with crystallizing melt (*e.g.*, Holness *et al.*, 2011) during cooling. The growth of cordierite at the expense of garnet points to a pressure decrease during D_2.

5.2.2 Migmatitic grey gneiss (SP3B)

Macroscopically, the rock is a grey banded gneiss with a synmigmatitic foliation S_1 marked by the alternation of leucosome and melanosome layers (Fig. 5b). This foliation is transposed into a subvertical, N040-striking foliation S_2, marked by alternating quartzo-feldspathic and biotite-rich layers, several mm up to 1 cm thick, which correspond to the leucosome and melanosome, respectively. Locally, significantly coarser-grained quartzo-feldspathic leucosomes, up to 10 cm thick, are present with a spacing generally of 20–50 cm. They are in general parallel to the S_2 foliation, but are localized also in necks of foliation boudins and shear bands. The sample comprises garnet, biotite, plagioclase (An29–38), quartz and ilmenite. Biotite (X_{Mg} = 0.48–0.54, Ti = 0.14 a.p.f.u.; Fig. 6b) is aligned parallel to the layering of the sample, but also commonly crystallizes in the fractures and at the rims of garnet (Fig. 6b). Garnet (up to 2 mm) is anhedral, almandine-rich and displays an unzoned core and markedly zoned rim, characterized by rimward decrease of pyrope and X_{Mg} and increase of spessartine (Alm65→68 Prp16→8 Grs6 Sps 11→21, X_{Mg} = 0.19→0.11; Fig. 7b). Monazite commonly forms crystal aggregates elongated parallel to the foliation S_2 (Fig. 6b), and locally occurs as inclusions in garnet. Numerous grains of zircon are included in biotite, plagioclase and garnet.

The equilibrium mineral assemblage comprises garnet, biotite, plagioclase, quartz and ilmenite, interpreted as contemporaneous with S_1. Garnet zoning suggests diffusional reequilibration due to partial resorption of previously chemically homogeneous crystals during D_2.

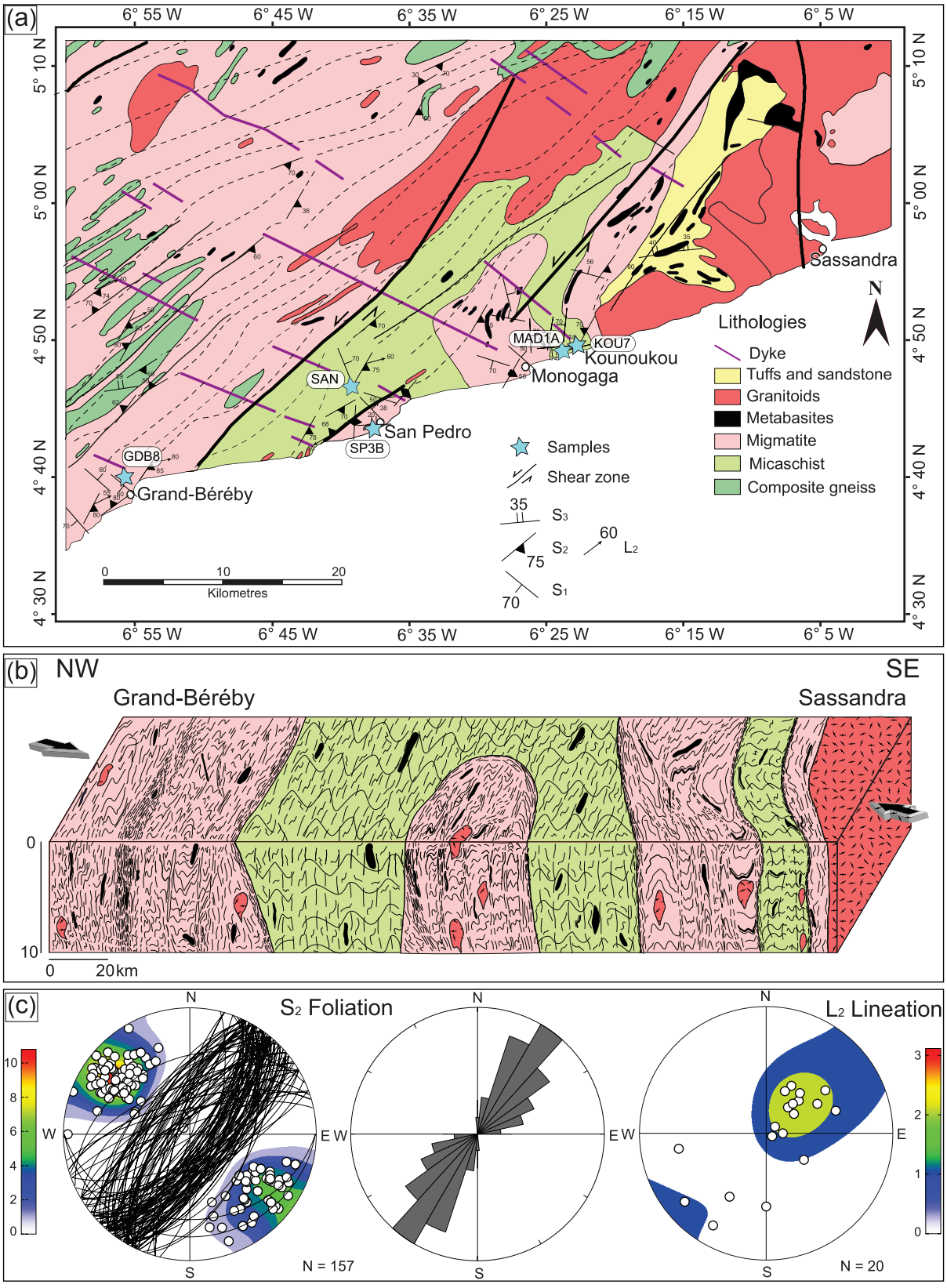

Fig. 4. Detailed geological map with structural relationships. (a) Structural map showing the orientation of S_1, S_2 and S_3 foliations. L_2 lineations are also plotted. (b) Geological cross-section showing the D_2 deformation phase. (c) Equal-area, lower hemisphere stereoplots show D_2 planar (foliation S_2) and linear (lineation L_2) deformation features.

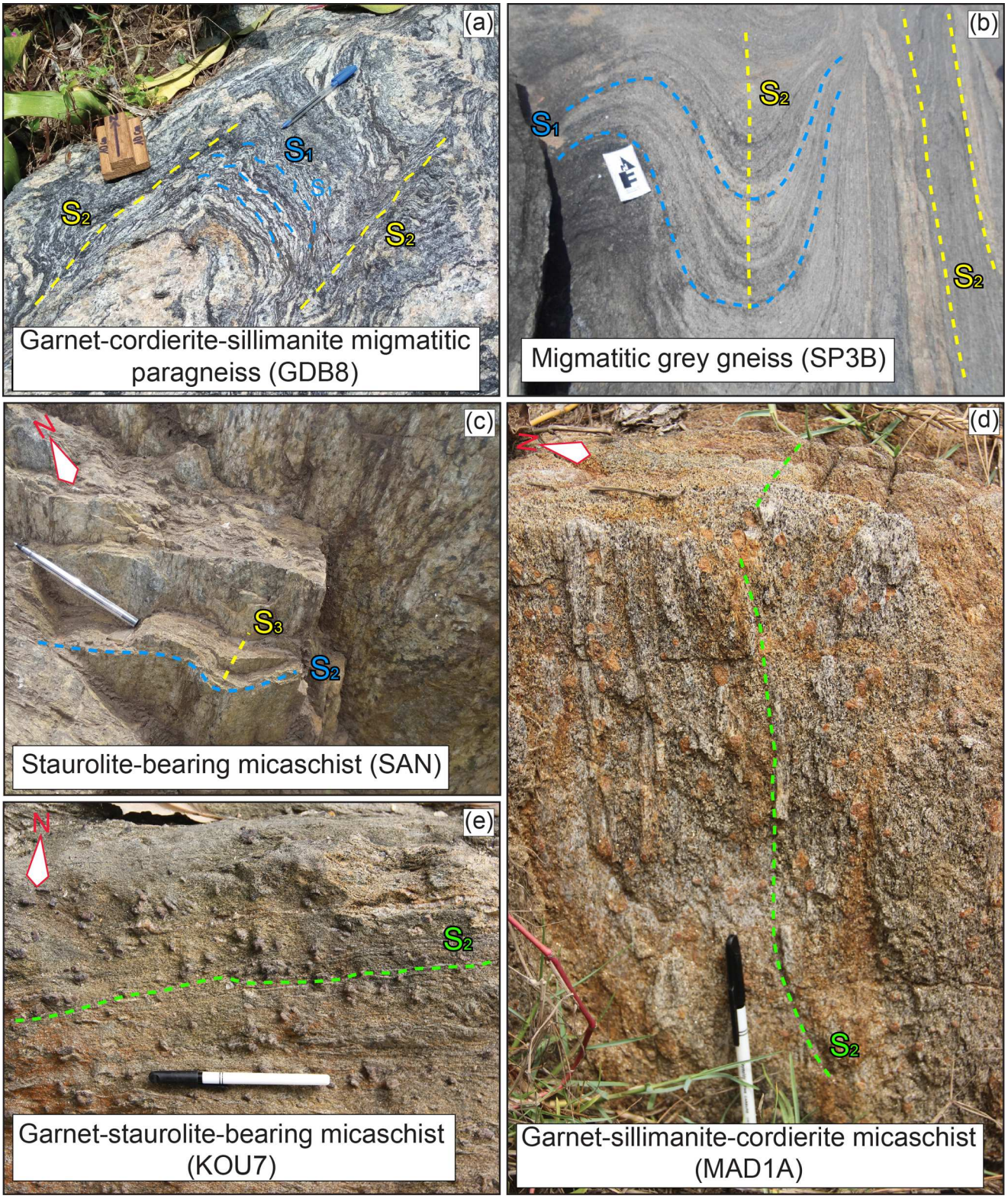

Fig. 5. Field photographs illustrating typical structural relationships (S_1, S_2 and S_3) in this study. (a) S_1 and S_2 in garnet–cordierite–sillimanite migmatitic paragneiss Grand-Béréby (GDB8). (b) S_1 and S_2 in migmatitic grey gneiss San Pedro (SP3B). (c) S_1 and S_2 in staurolite-bearing micaschist San Pedro (SAN). (d) S_2 in garnet–sillimanite–cordierite micaschist Madie (MAD1A). (e) S_3 in garnet–staurolite-bearing micaschist Kounoukou (KOU7).

Table 3a. Representative microprobe analyses of selected minerals.

Samples	GDB8											SP3B					SAN				
Mineral	g		g		bi			pl		cd		g		bi	pl	st	bi		pl	mu	chl
Position	Rim	Core	Rim	Core	in g	in cd	matrix	in g	matrix	in g	matrix	Rim	Core				Rim	Core			
SiO_2	38.24	39.85	38.17	37.98	36.89	36.01	35.85	62.37	61.75	49.93	50.43	37.22	36.76	35.82	60.20	24.62	36.84	36.75	63.31	45.78	26.06
TiO_2	0.00	0.00	0.01	0.00	5.13	4.00	4.99	0.01	0.00	0.00	0.00	0.00	0.00	2.48	0.00	0.39	1.41	1.35	0.00	0.42	0.09
Al_2O_3	20.86	21.65	22.23	21.75	16.22	17.60	15.50	23.82	23.64	33.52	33.69	21.04	20.65	17.53	24.52	48.01	19.28	18.87	23.49	35.03	23.26
Fe_{tot} as FeO	31.16	27.79	28.24	28.57	8.74	14.82	14.91	0.05	0.06	3.53	4.48	29.18	30.24	18.47	0.07	21.56	14.99	15.45	0.12	2.18	18.48
MnO	2.09	1.7	2.46	2.43	0.00	0.07	0.11	0.00	0.02	0.06	0.08	8.46	7.02	0.26	0.01	0.75	0.14	0.20	0.00	0.00	0.30
MgO	6.05	9.06	8.22	8.31	17.13	12.59	12.76	0.02	0.00	11.30	10.87	2.68	3.11	10.06	0.00	1.71	12.41	12.17	0.00	0.49	17.92
CaO	0.99	0.94	0.94	0.85	0.00	0.00	0.00	5.37	5.33	0.04	0.02	2.11	2.08	0.00	6.91	0.00	0.01	0.00	4.58	0.00	0.04
Na_2O	0.00	0.05	0.00	0.00	0.19	0.04	0.96	9.45	9.15	0.04	0.06	0.00	0.05	0.05	8.48	0.01	0.25	0.28	8.92	1.52	0.11
K_2O	0.01	0.02	0.00	0.03	9.98	10.02	9.77	0.33	0.24	0.00	0.01	0.01	0.01	9.99	0.09	0.00	9.03	9.4	0.03	8.99	0.54
Cr_2O_3	0.01	0.02	0.03	0.01	0.02	0.09	0.01	0.00	0.00	0.00	0.00	0.01	0.00	0.02	0.00	0.03	0.04	0.00	0.01	0.00	0.04
BaO	b.d.l	b.d.l	b.d.l	b.d.l	0.18	0.15	0.19	0.00	0.00	0.00	0.00	0.00	0.00	0.32	0.00	0.00	0.11	0.14	0.00	0.45	0.00
Total	99.41	101.07	100.3	99.95	95.43	96.29	95.08	101.42	100.19	98.42	99.65	100.72	99.92	95.38	100.27	97.07	95.21	94.96	100.46	94.86	86.89
ox	12	12	12	12	11	11	11	8	8	18	18	12	12	11	8	46	11	11	8	22	14
Si	3.03	3.04	2.96	2.96	2.71	2.70	2.71	2.74	2.74	5.02	5.03	2.98	2.97	2.74	2.68	7.26	2.75	2.76	2.79	3.07	2.68
Ti	0.00	0.00	0.00	0.00	0.28	0.23	0.28	0.00	0.00	0.00	0.00	0.00	0.00	0.14	0.00	0.09	0.08	0.08	0.00	0.02	0.01
Al	1.95	1.95	2.03	2.00	1.41	1.55	1.38	1.23	1.24	3.97	3.96	1.99	1.96	1.58	1.29	16.70	1.70	1.67	1.22	2.77	2.82
Cr	0.00	0.00	0.00	0.00	0.00	0.01	0.00	0.00	0.00	0.00	0.00	0.00	0.00	0.00	0.00	0.00	0.00	0.00	0.00	0.00	0.00
Fe^{3+}	0.00	0.00	0.06	0.09	0.00	0.00	0.00	0.00	0.00	0.00	0.00	0.05	0.11	0.00	0.00	0.00	0.00	0.00	0.00	0.00	0.00
Mg	0.72	1.03	0.95	0.96	1.88	1.41	1.44	0.00	0.00	1.69	1.62	0.32	0.37	1.15	0.00	0.75	1.38	1.36	0.00	0.05	2.74
Fe^{2+}	2.07	1.77	1.77	1.76	0.54	0.93	0.94	0.00	0.00	0.30	0.37	1.91	1.91	1.18	0.00	3.36	0.94	0.97	0.00	0.12	1.59
Mn	0.14	0.11	0.16	0.16	0.00	0.01	0.01	0.00	0.00	0.01	0.01	0.57	0.48	0.02	0.00	0.19	0.01	0.01	0.00	0.00	0.03
Ca	0.08	0.08	0.08	0.07	0.00	0.00	0.00	0.25	0.25	0.00	0.00	0.18	0.18	0.00	0.33	0.00	0.00	0.00	0.22	0.00	0.00
Ba					0.01	0.00	0.01	0.00	0.00	0.00	0.00	0.00	0.00	0.01	0.00	0.00	0.00	0.00	0.00	0.01	0.00
Na	0.00	0.01	0.00	0.00	0.03	0.01	0.14	0.81	0.79	0.01	0.01	0.00	0.01	0.01	0.73	0.00	0.04	0.04	0.76	0.20	0.02
K	0.00	0.00	0.00	0.00	0.94	0.96	0.94	0.02	0.01	0.00	0.00	0.00	0.00	0.98	0.01	0.00	0.86	0.90	0.00	0.77	0.07
OH					1.78	1.79	1.99							1.91			1.83	1.92		2.00	7.99
F					0.22	0.21	0.00							0.09			0.17	0.08		0.00	0.00
Cl					0.00	0.00	0.00							0.00			0.00	0.00		0.00	0.01
Total	7.99	7.99	8.00	8.00	9.78	9.78	9.86	5.05	5.04	11.00	11.00	8.00	8.00	9.81	5.04	28.35	9.77	9.80	4.99	9.01	17.95

Table 3a. (continued).

Samples	GDB8										SP3B					SAN					
Mineral	g		g		bi		pl		cd		g		bi	pl	st	bi		pl	mu	chl
Position	Rim	Core	Rim	Core	in g	in cd	matrix	in g	matrix	in g	matrix	Rim	Core				Rim	Core			
XAlm	0.69	0.59	0.60	0.59								0.64	0.65								
XPrp	0.24	0.34	0.32	0.33								0.11	0.13								
XGrs	0.03	0.02	0.03	0.02								0.06	0.06								
XSps	0.05	0.04	0.05	0.05								0.19	0.16								
X_{Mg}	0.26	0.37	0.35	0.35	0.78	0.61	0.60			0.85	0.81	0.14	0.16	0.49		0.12	0.60	0.58			0.63
X_{an}								0.23	0.24						0.31				0.22		
X_{ab}								0.75	0.75						0.69				0.78		
X_{or}								0.02	0.01						0.00				0.00		

5.2.3 Staurolite-bearing micaschist (SAN)

Macroscopically, the micaschist displays a composite foliation S_2 weakly folded by open folds with S_3 axial planes (Fig. 5c). Microscopically, S_2 is defined by the preferred orientation of biotite (up to 3 mm; X_{Mg} = 0.58–0.62; Al = 1.58–1.74 a.p.f.u.; Ti = 0.06–0.09 a.p.f.u.), chlorite (X_{Mg} = 0.62–0.65, Al = 2.71–2.86 a.p.f.u.), plagioclase (An21–23) and quartz (Fig. 6c). The foliation contains magnetite and ilmenite and slightly wraps around euhedral to subhedral synkinematic porphyroblasts of staurolite (up to 2.5 mm; X_{Mg} = 0.19–0.22, Ti = 0.09–0.12 a.p.f.u., Mn = 0.17–0.24 a.p.f.u.) and andalusite (up to 10 mm), which commonly contain sigmoidal inclusion trails of quartz, continuous with the S_2 foliation (Fig. 6c). Andalusite includes ilmenite, magnetite, quartz, biotite and locally anhedral crystals of staurolite. Rare fibrous sillimanite locally occurs parallel to the main foliation.

5.2.4 Garnet–sillimanite–cordierite micaschist (MAD1A)

The micaschist (Fig. 5d) is rich in quartz and plagioclase (An32–34) and displays a foliation S_2 marked by the preferred orientation of biotite (X_{Mg} = 0.52–0.60; Al = 1.67–1.72 a.p.f.u.; Ti = 0.05–0.10 a.p.f.u.) and abundant fibrous sillimanite (Fig. 6d). Anhedral garnet (up to 2 mm) has a relatively homogeneous core (Alm72–74 Prp15–17 Grs4–5 Sps7, X_{Mg} = 0.17–0.19) and a slightly zoned rim characterized by a rimward decrease of pyrope and X_{Mg}, and an increase of almandine and spessartine (Alm75 Prp12 Grs5 Sps8, X_{Mg} = 0.14; Figs. 6e and 7c). Rare staurolite (X_{Mg} = 0.19–0.20) is either included in plagioclase or at contact with garnet (Fig. 6e). Cordierite (X_{Mg} = 0.68–0.70; Na = 0.07 a.p.f.u.) is in contact with fibrous sillimanite and biotite. Accessory minerals include tourmaline, ilmenite, zircon and monazite.

The main syntectonic equilibrium mineral assemblage is inferred to comprise cordierite, sillimanite, biotite, plagioclase, quartz and ilmenite, and typifies low-pressure high-temperature metamorphic conditions. Garnet rims may or may not belong to this assemblage. Garnet zoning suggests diffusional reequilibration due to partial resorption of previously chemically homogeneous crystals. Rare staurolite suggests an earlier metamorphic stage of the Barrovian, medium-pressure type.

5.2.5 Garnet–staurolite-bearing micaschist (KOU7)

A macroscopically dark-coloured micaschist from Kounoukou (Fig. 5e) consists of garnet, staurolite, biotite, plagioclase, quartz, ilmenite and tourmaline (Figs. 6f and 6g). The main foliation S_2 is marked by the preferred orientation of biotite (X_{Mg} = 0.49–0.53), quartz and plagioclase (An29–32), and is weakly folded by open folds with S_3 axial planes. The foliation weakly wraps around subhedral porphyroblasts of garnet and staurolite (up to 3 mm). Poikiloblastic staurolite (X_{Mg} = 0.16–0.20) contains abundant quartz inclusion trails that mark the foliation S_1, oblique to the matrix foliation S_2. The chemical zoning of garnet is characterized by a rimward decrease of pyrope, X_{Mg} and spessartine, and an increase of almandine, whereas the proportion of grossular remains constant (Alm74→81, Prp13→11, Grs4, Sps8→4, X_{Mg} = 0.16→0.12; Fig. 7d). Garnet chemical zoning is interpreted to reflect prograde growth.

Table 3b. Representative microprobe analyses of selected minerals.

Samples	MAD1A							KOU7					
Mineral	g		st		bi	pl	cd	g		st		bi	pl
Position	Rim	Core	g selvedge	in pl				Rim	Core	Matrix	in pl		
SiO_2	37.40	37.57	26.88	27.84	36.20	60.14	48.72	37.57	36.95	27.20	27.46	35.73	60.65
TiO_2	0.00	0.02	0.55	0.74	1.77	0.00	0.00	0.00	0.04	0.64	0.59	1.21	0.00
Al_2O_3	21.55	21.78	53.28	52.75	18.67	25.23	32.64	21.53	21.34	53.64	52.67	27.37	24.92
Fe_{tot} as FeO	33.60	33.13	13.21	13.04	17.61	0.02	7.10	35.66	33.68	14.29	14.47	16.20	0.02
MnO	3.32	3.22	0.20	0.17	0.08	0.05	0.19	1.44	3.36	0.10	0.10	0.00	0.00
MgO	3.37	3.92	1.78	2.24	10.75	0.00	8.52	3.24	3.35	1.77	1.66	7.80	0.00
CaO	1.52	1.62	0.00	0.03	0.00	7.15	0.05	1.48	1.40	0.02	0.00	0.00	6.55
Na_2O	0.02	0.01	0.00	0.04	0.25	7.45	0.50	0.01	0.04	0.00	0.04	0.18	8.12
K_2O	0.00	0.01	0.00	0.00	8.97	0.05	0.01	0.00	0.04	0.00	0.00	6.86	0.05
Cr_2O_3	0.00	0.03	0.37	0.18	0.11	0.00	0.00	0.04	0.01	0.05	0.27	0.00	0.01
BaO	0.00	0.00	0.00	0.00	0.22	0.00	0.00	0.00	0.00	0.00	0.00	0.20	0.00
Total	100.77	101.33	96.26	97.02	94.95	100.08	97.73	100.97	100.21	97.71	97.25	95.81	100.33
ox	12	12	46	46	11	8	18	12	12	46	46	11	8
Si	2.98	2.97	7.58	7.77	2.75	2.67	5.03	2.99	2.97	7.59	7.70	2.60	2.69
Ti	0.00	0.00	0.12	0.15	0.10	0.00	0.00	0.00	0.00	0.13	0.12	0.07	0.00
Al	2.03	2.03	17.71	17.36	1.67	1.32	3.97	2.02	2.02	17.63	17.42	2.34	1.30
Cr	0.00	0.00	0.08	0.04	0.01	0.00	0.00	0.00	0.00	0.01	0.06	0.00	0.00
Fe^{3+}	0.02	0.04	0.00	0.00	0.00	0.00	0.00	0.00	0.06	0.00	0.00	0.00	0.00
Mg	0.40	0.46	0.75	0.93	1.22	0.00	1.31	0.39	0.40	0.74	0.69	0.85	0.00
Fe^{2+}	2.22	2.15	2.61	2.38	1.12	0.00	0.61	2.37	2.20	2.69	2.70	0.98	0.00
Mn	0.22	0.22	0.05	0.04	0.01	0.00	0.02	0.10	0.23	0.02	0.02	0.00	0.00
Ca	0.13	0.14	0.00	0.01	0.00	0.34	0.01	0.13	0.12	0.01	0.00	0.00	0.31
Ba	0.00	0.00	0.00	0.00	0.01	0.00	0.00	0.00	0.00	0.00	0.00	0.01	0.00
Na	0.00	0.00	0.00	0.02	0.04	0.64	0.10	0.00	0.01	0.00	0.02	0.03	0.70
K	0.00	0.00	0.00	0.00	0.87	0.00	0.00	0.00	0.00	0.00	0.00	0.64	0.00
OH					1.92							1.94	
F					0.08							0.06	
Cl					0.00							0.00	
Total	8.00	8.00	28.90	28.71	9.77	4.99	11.04	8.00	8.00	28.82	28.75	9.50	5.01
XAlm	0.75	0.73						0.80	0.75				
XPrp	0.13	0.16						0.13	0.14				
XGrs	0.04	0.05						0.04	0.04				
XSps	0.08	0.07						0.03	0.08				
X_{Mg}	0.15	0.18	0.19	0.23	0.52		0.68	0.14	0.15	0.18	0.17	0.46	
X_{an}						0.35							0.31
X_{ab}						0.65							0.69
X_{or}						0.00							0.00

b.d.l: below detection limit

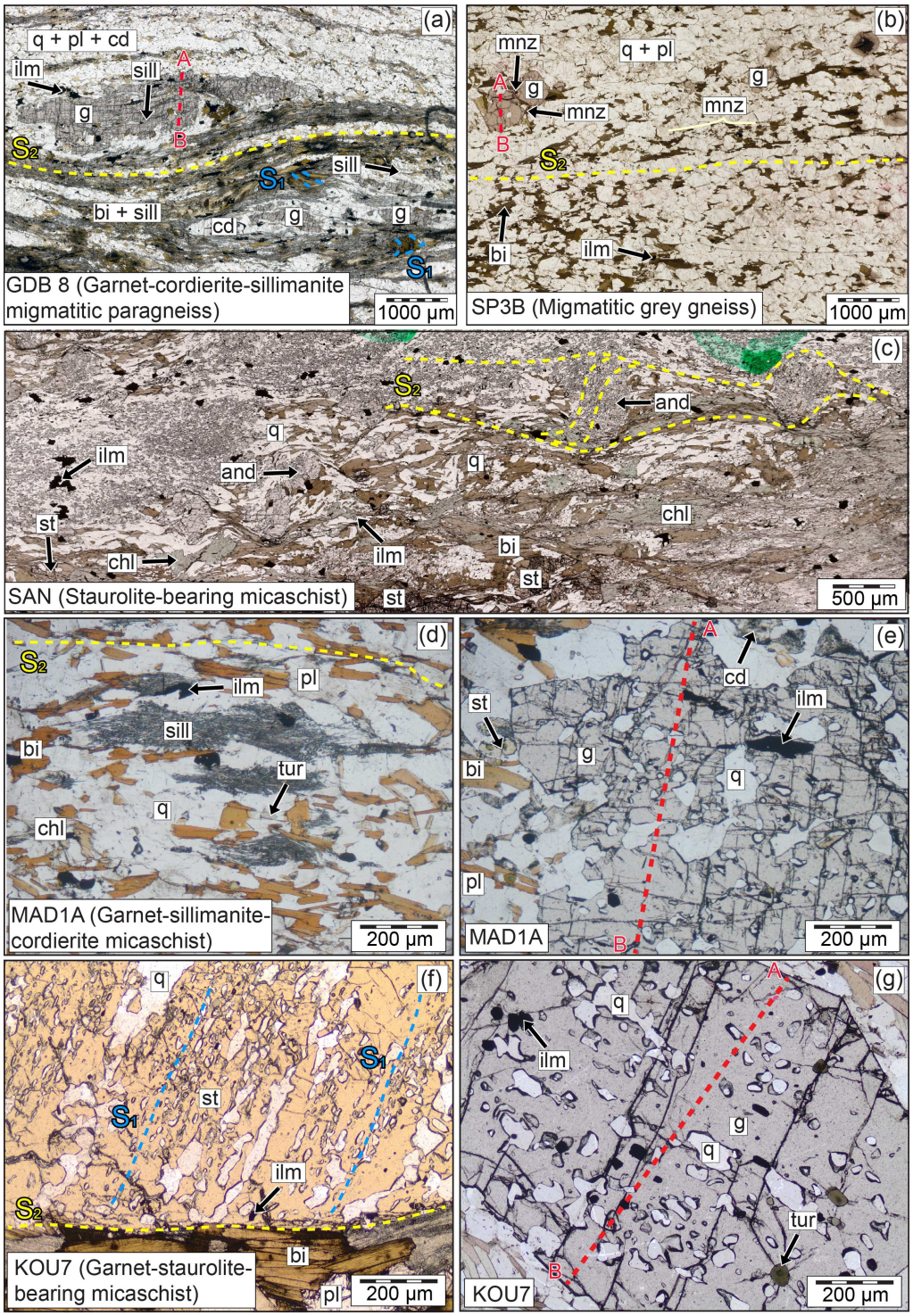

Fig. 6. Photomicrographs (plane polarized light). (a) Sample GDB8. Main penetrative foliation S_2 (fine-grained biotite + prismatic sillimanite) wraps around (a) a microlithon with preserved foliation S_1 marked by coarse-grained biotite and prismatic sillimanite, and anhedral porphyroblasts of garnet with abundant inclusions of fine sillimanite needles. The dashed line A-B indicates the location of the chemical profile of garnet (Fig. 7a). Sample SP3B: (b) String of monazite crystals aligned parallel to the foliation S_2 marked by biotite, which also crystallizes in the fractures and at the rims of garnet porphyroblasts containing inclusions of monazite. A-B indicates the location of the chemical profile of garnet (Fig. 7b). Sample SAN: (c) Biotite and rare fibrous sillimanite mark the main foliation (S_2) and (d) andalusite replaced partly by chlorite. Sample MAD1A: (e) Foliation S_2 marked by biotite and clusters of fibrous sillimanite. (f) Garnet porphyroblast in contact with rare staurolite crystals. The dashed line A-B indicates the location of the chemical profile (Fig. 7c). Sample KOU7: (g) Staurolite contains quartz inclusion trails that mark the foliation S_1, oblique to the matrix foliation S_2. (h) A-B – Location of the chemical profile (Fig. 7d) across a garnet porphyroblast with inclusions of ilmenite and quartz.

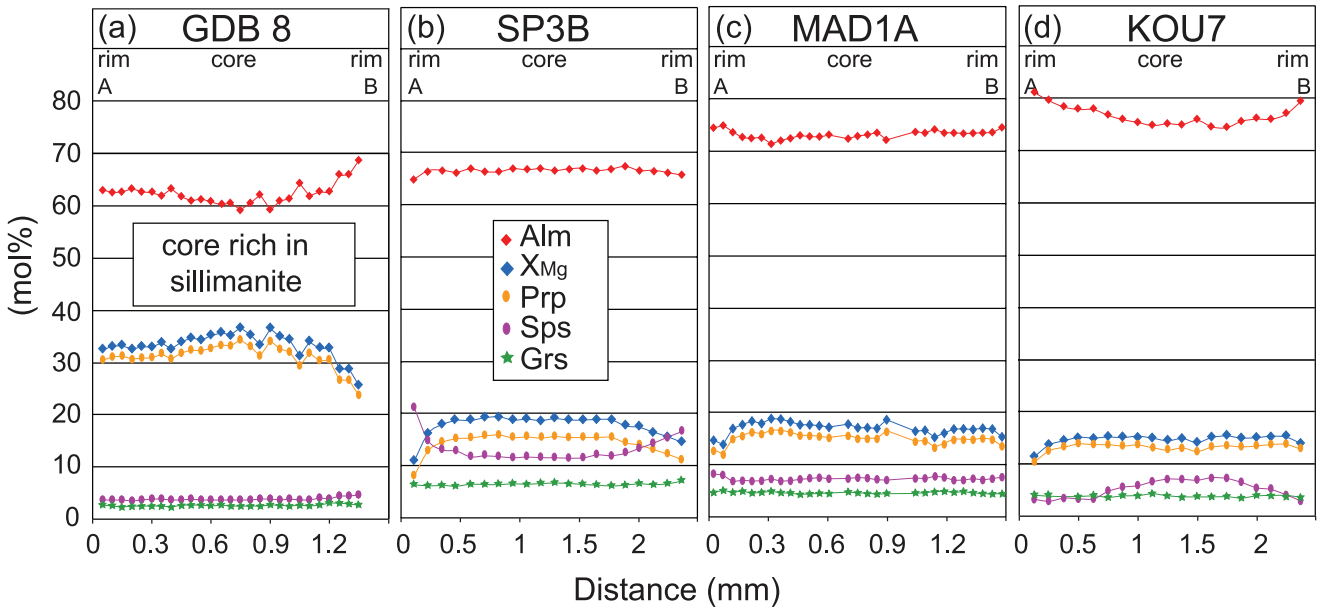

Fig. 7. Chemical profiles of garnet (mole %). Location is shown in Figures 6a (GDB8), 6b (SP3B), 6e (MAD1A) and 6g (KOU7).

5.3 Metamorphic conditions and P–T paths

5.3.1 Garnet–cordierite–sillimanite migmatitic paragneiss (GDB8)

In the P–T pseudosection (Fig. 8a), the inferred peak mineral assemblage garnet, biotite, sillimanite, plagioclase, quartz, ilmenite, and melt is stable at pressures higher than ca. 7 kbar (limited at low pressure by the appearance of cordierite) and temperatures in excess of 690 °C (limited by the solidus at the low-temperature side). The upper P limit is given by the sillimanite–kyanite transition. The increase of the sillimanite grain size from the garnet core to the matrix testifies to crystallisation during an increase in temperature. The constant amount of grossular indicates that the prograde P–T evolution was parallel to the position of the grossular isopleths. The composition of the garnet core ($X_{Mg}(g) = 0.34$; Grs2–3), most susceptible to represent the peak metamorphic composition, compared to the position of the calculated compositional isopleths of garnet, suggest peak metamorphic pressure and temperature at ca. 10 kbar, 820 °C. The subsequent crystallisation of cordierite at the expense of garnet, compatible with the observed rimward decrease of the garnet X_{Mg} (0.37→0.26), suggests progressive reequilibration during a pressure decrease down to ca. 6 kbar, probably followed by cooling below the solidus. The homogeneous composition of matrix biotite ($X_{Mg} = 0.60$) suggests subisobaric cooling, parallel to the corresponding isopleths in the field g–bi–cd–ilm–liq–sill (+q + pl).

5.3.2 Migmatitic grey gneiss (SP3B)

In the P–T pseudosection (Fig. 8b), the mineral assemblage of the migmatitic grey gneiss SP3B, g-ilm-q-pl-bi with or without melt, is stable at $T > 620$ °C and $P > 5$ kbar, limited by the appearance of staurolite towards low temperatures and cordierite towards low pressures. Comparing the calculated compositional isopleths with the observed composition of the homogeneous garnet core ($X_{Mg}(g) = 0.19$, Grs6), inferred to represent the composition equilibrated at the metamorphic peak, the equilibration conditions can be constrained at ca. 8–9 kbar, 650–700 °C. The prograde P–T path could not have been established due to the lack of mineral inclusions or any other relics of prograde assemblages. The chemical zoning of the garnet rim is compatible with decompression and/or cooling, but does not allow precise estimation of the retrograde P–T path.

5.3.3 Staurolite-bearing micaschist (SAN)

The syn-S_2 assemblage of the micaschist is stable in the field st–and–pl–bi–chl–ilm–mt (+q + H_2O at 560–580 °C, 3.5–4 kbar, limited by the disappearance of chlorite towards high temperatures, the disappearance of staurolite towards low pressures and the appearance of paragonite towards low temperatures and high pressures (Fig. 9a). The observation of rare sillimanite needles in the sample suggests that the rocks would have passed through the stability field of sillimanite before, possibly due to decompression from a higher-pressure syn-S_1 peak.

5.3.4 Garnet–sillimanite–cordierite micaschist (MAD1A)

In the pseudosection, calculated in the model system MnNCKFMASHTO (Fig. 9b), the dominant syn-S_2 assemblage pl-g-ilm-cd-sill (+q + bi + H_2O) corresponds to a field at 5–6 kbar, 620–690 °C. If garnet rims were not in equilibrium with the other minerals, the syn-S_2 assemblage cd-sill-pl-ilm would indicate lower pressures and temperatures (dashed arrow in Fig. 9b). The former stability of staurolite with garnet suggests higher pressures (5–9 kbar). The isopleth for grossular (Grs5) points to a pressure range of 7–8 kbar, for temperatures of ~ 620–650 °C. Other compositional isopleths

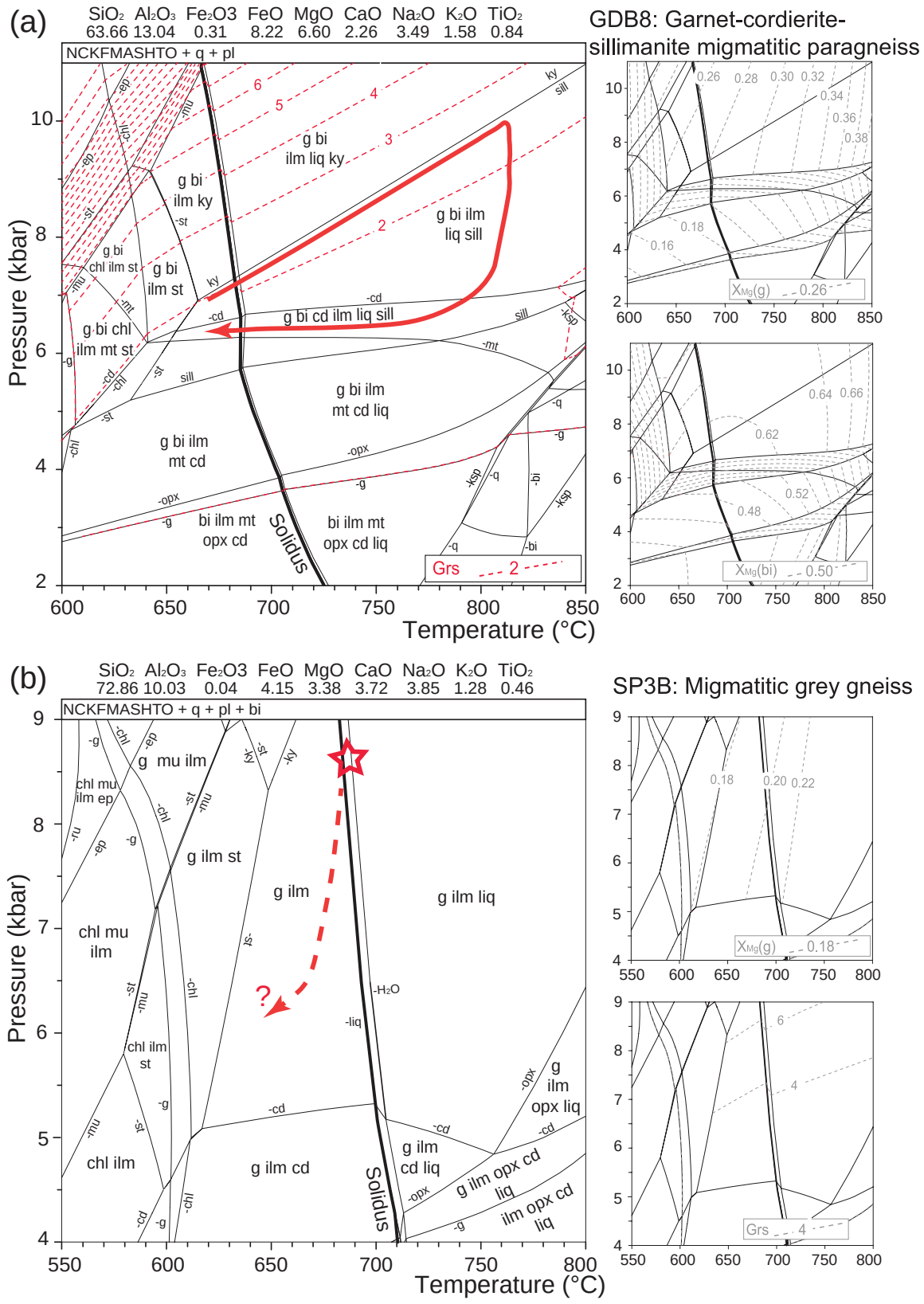

Fig. 8. P–T pseudosections in the model system NCKFMASHTO (whole-rock compositions expressed in mole %) and compositional isopleths for (a) the migmatitic paragneiss GDB8 and (b) the migmatitic grey gneiss SP3B. Red arrow and red star show the inferred P–T path (GDB8) and the equilibration P–T conditions (SP3B), respectively. Field limits are marked by the phase that appears/disappears. See text for details.

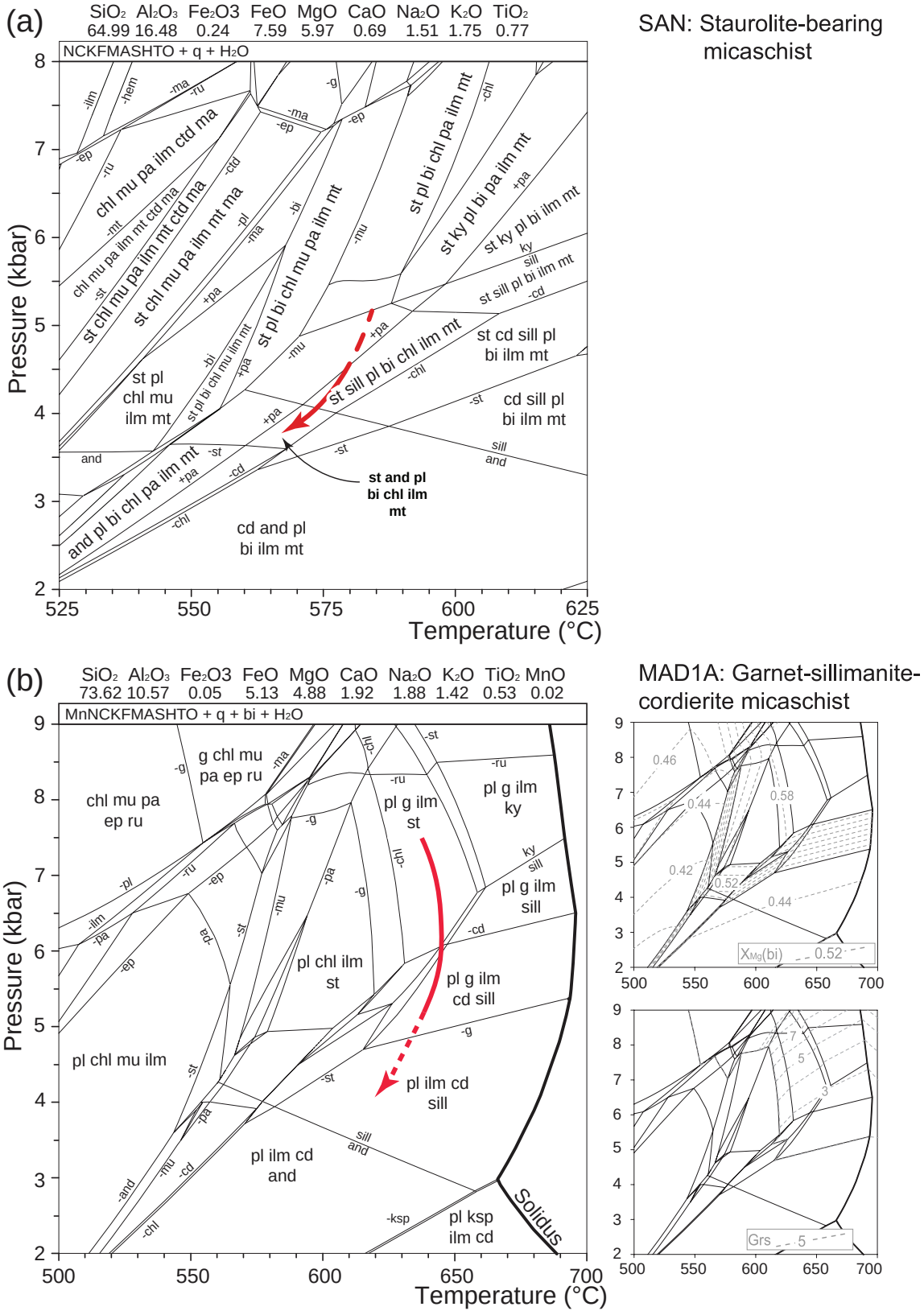

Fig. 9. P–T pseudosections and compositional isopleths calculated for the samples (a) SAN in the model system NCKFMASHTO, and (b) MAD1A in the model system MnNCKFMASHTO. Red arrows show the inferred P–T paths. See text for details.

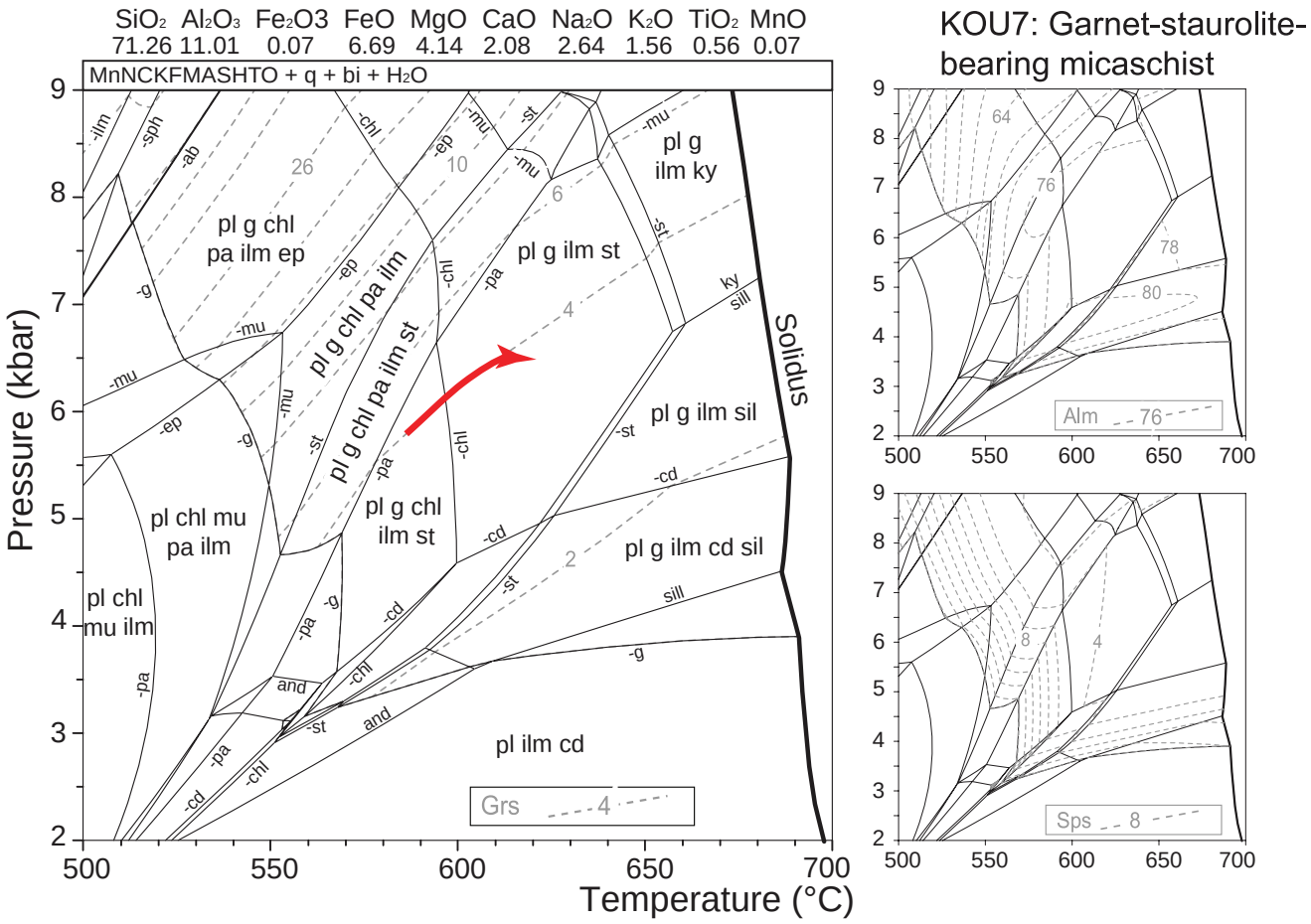

Fig. 10. P–T pseudosection (MnNCKFMASHTO) and compositional isopleths calculated from the sample KOU7 (whole-rock composition expressed in mole %). Red arrow shows the inferred P–T paths. See text for details.

are not very helpful in constraining better the equilibration P–T conditions. Although the values globally fit with the observations in the inferred stability fields, the range of the observed mineral compositions is larger than those fields. Garnet rim zoning (Alm72→75 Prp16→12 Sps7→8, X_{Mg} = 0.18→0.14) is compatible with a P–T evolution dominated by a pressure decrease.

5.3.5 Garnet–staurolite-bearing micaschist (KOU7)

In the pseudosection calculated in the model system MnNCKFMASHTO (Fig. 10), the observed syn-S_2 assemblage pl-g-ilm-st (+q + bi + H_2O) is stable at 5–8 kbar, 600–650 °C. The intersection of the calculated compositional isopleths suggests that the garnet core (Alm74 Grs4 Sps8) started the crystallisation in the neighbouring lower-temperature chlorite-bearing field at ca. 5.8 kbar and 585 °C. The progressive rimward decrease of the proportion of spessartine, while the proportion of grossular remains constant, suggests a prograde up-pressure up-temperature evolution, sub-parallel to the isopleth of the grossular content. It peaks in the g–st–pl–ilm field where the isopleths corresponding to the composition of the garnet rim (Grs4, Sps4) intersect at ca. 6.6 kbar, 620 °C.

5.4 U–Pb *in situ* dating of monazite

5.4.1 Garnet–cordierite–sillimanite migmatitic paragneiss (GDB8)

In GDB8, monazite crystals (ca. 100 μm) are in contact with or included in crystals of biotite and plagioclase (Fig. 11a). Fifteen analyses were performed on eleven monazite crystals, among which eleven are close to concordant (concordance > 95%) and cluster into two groups with distinct ages. The main group of concordant analyses provides a $^{207}Pb/^{206}Pb$ weighted mean age of 2040 ± 6 Ma (MSWD = 0.1, N = 8). Three other analyses are significantly younger and yield a $^{207}Pb/^{206}Pb$ weighted mean age of 2003 ± 12 Ma (MSWD = 0.2, N = 3) (Fig. 12c).

5.4.2 Migmatitic grey gneiss (SP3B)

Monazite in SP3B has a variable size, ranging from 10 to 100 μm. It commonly forms clusters aligned parallel to S_2 (Fig. 11b). Under BSE imaging, some grains reveal contrasting areas showing complex zonations (Figs. 11f and 11g). X-ray maps were performed on three grains (≥ 50 μm) in order to assess the internal distribution of the chemical elements and

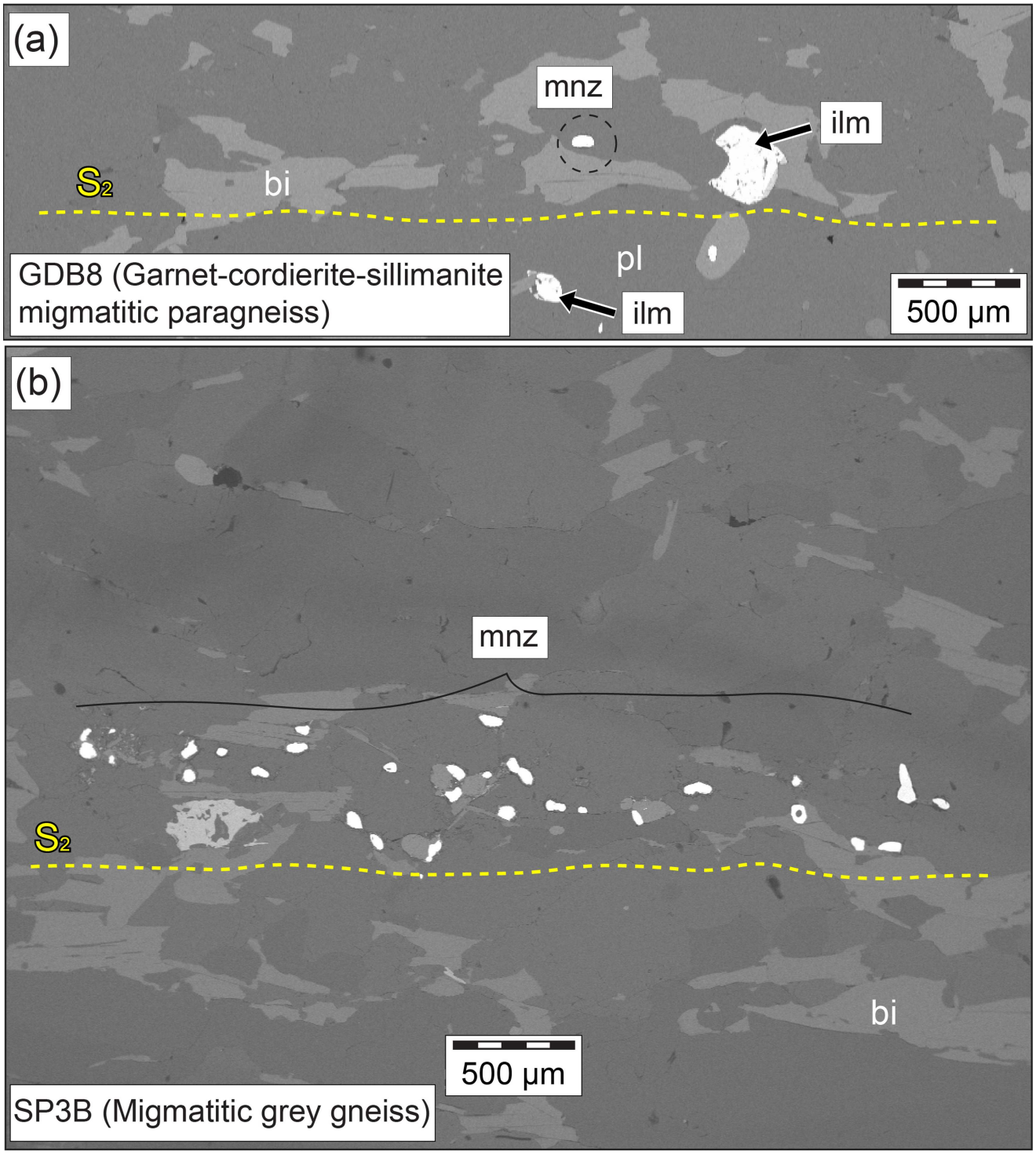

Fig. 11. (a) Position of the monazite crystals (bright spots) in the thin section GDB8. (b) Alignment of monazite clusters parallel to S_2 in migmatitic grey gneiss SP3B. (c–g) Migmatitic grey gneiss SP3B. (c) Back-scattered electron (BSE) images showing the position of the monazite crystals (bright spots) with respect to the garnet porphyroblasts. (d, e) Microprobe X-ray maps and (f, g) BSE images with analytical spots and associated $^{207}Pb/^{206}Pb$ dates of monazite grain marked in (a). LC: low concentration; HC: high concentration.

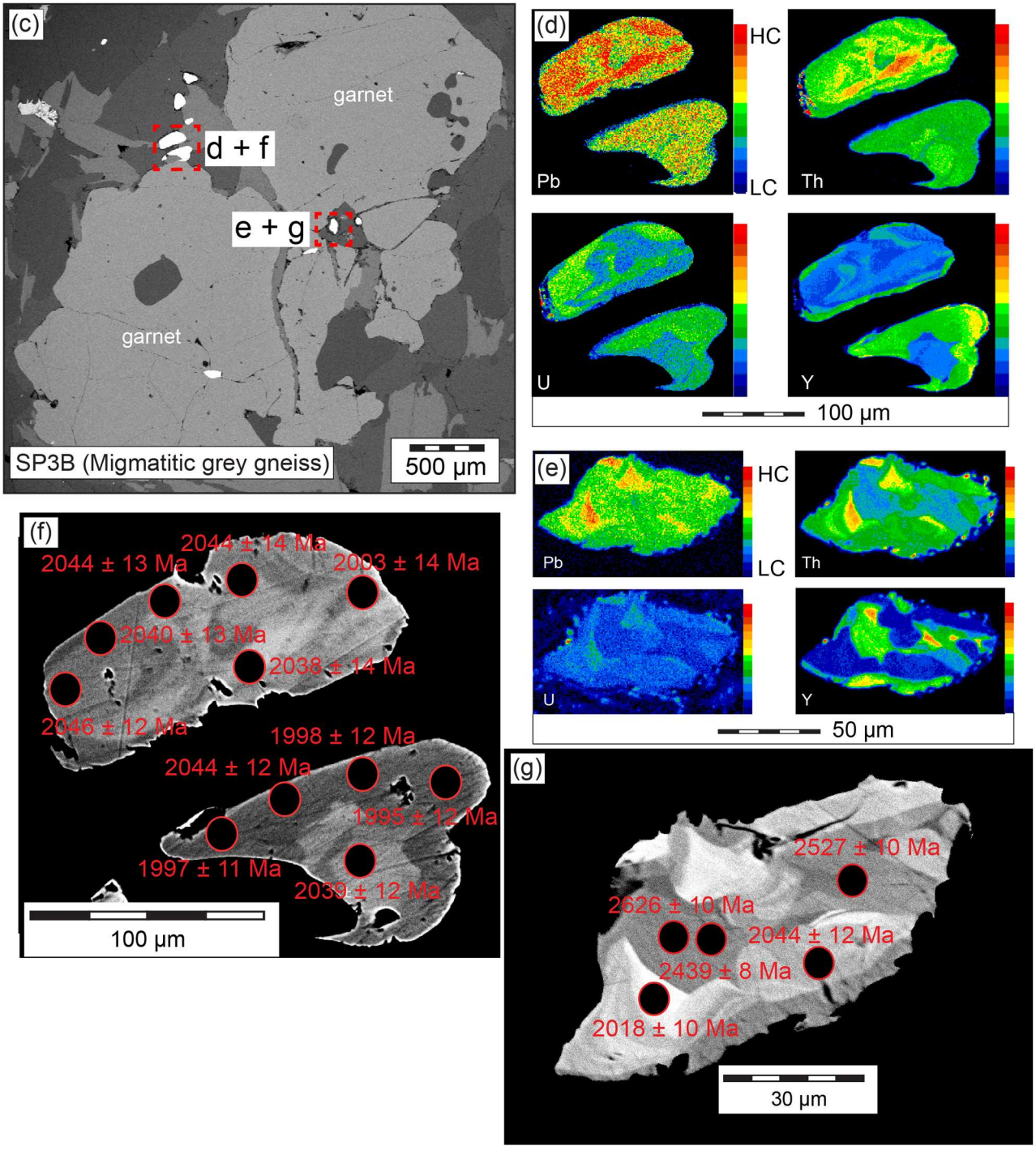

Fig. 11. (Continued)

target U–Pb analyses. Mapped crystals have distinct zones with a heterogeneous distribution of lead (Pb), thorium (Th), uranium (U) and yttrium (Y) (Figs. 11d and 11e). These irregular intra-grain zonations are interpreted as chemical fronts and suggest a redistribution of the elements at the subgrain scale. Eighty-one analyses were carried out on twenty-eight grains located in different textural positions in the thin section, included in either biotite, plagioclase or garnet (Table S2, see Supplementary Materials). Overall, analyses are distributed in two groups with sub-concordant to concordant data points (concordance ≥ 95%) at around 2040 and 2000 Ma, except for three analyses from the central part of one large grain in contact with garnet (Figs. 11f, 11g, 12a and 12b), which yield either discordant Archean dates (minimum dates at 2626 ± 19 Ma and 2527 ± 20 Ma) or a concordant date at 2439 ± 16 Ma (Fig. 12a). The main group of 46 analyses provides a $^{207}Pb/^{206}Pb$ weighted mean age of 2037 ± 2 Ma (MSWD = 0.79; N = 46) whereas the second group yields a

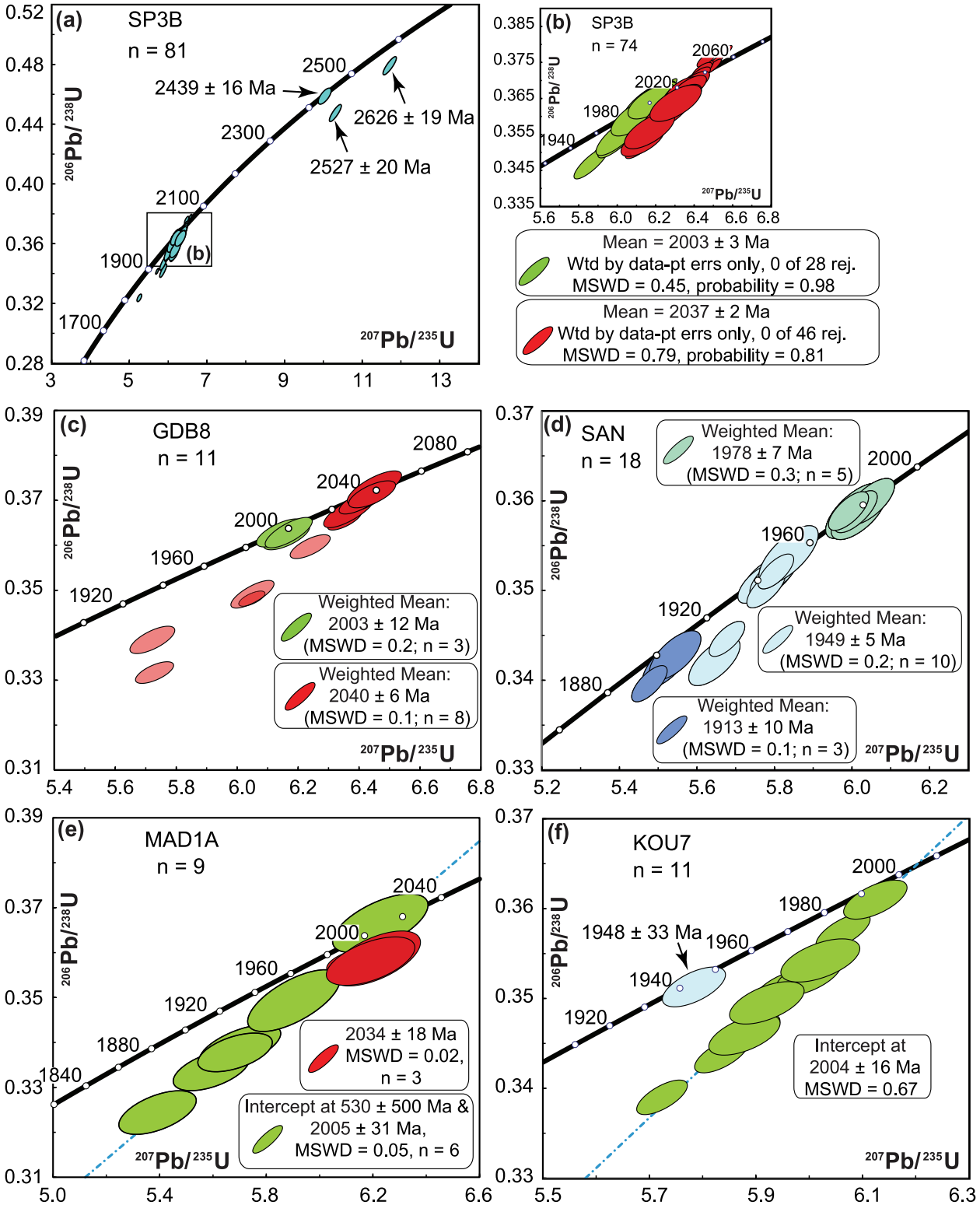

Fig. 12. U–Pb dating of monazites by LA-ICP-MS. (a) Concordia diagram showing all analytical points for monazites from the migmatitic grey gneiss SP3B. (b) Zoom of the concordia diagram showing the two age groups at ca. 2000 and 2037 Ma in the sample SP3B. (c–f) U–Pb concordia diagrams for monazites from garnet–cordierite–sillimanite migmatitic paragneiss GDB8 (c) and metapelites SAN, MAD1A and KOU7 (d, e and f respectively). SAN: staurolite-bearing micaschist; MAD1A: garnet–sillimanite–cordierite micaschist; KOU7: garnet–staurolite-bearing micaschist.

distinctly younger age of 2003 ± 3 Ma (MSWD = 0.45; *N* = 28). It is noteworthy that the 2037 ± 2 Ma-old group corresponds to monazites that are aligned parallel to the S_2 foliation (Fig. 11b).

5.4.3 Staurolite-bearing micaschist (SAN)

Monazite is small (ca. 10 μm) and either included in andalusite and biotite, or located along grain boundaries. Eighteen analyses have been performed on twelve monazite grains. All analyses cluster close to Concordia (≥ 95% concordance) and define three groups of ages yielding $^{207}Pb/^{206}Pb$ weighted mean ages of 1978 ± 7 Ma (MSWD = 0.3, *N* = 5), 1949 ± 5 Ma (MSWD = 0.2, *N* = 10) and 1913 ± 10 Ma (MSWD = 0.1, *N* = 3) (Fig. 12d).

5.4.4 Garnet–sillimanite–cordierite micaschist (MAD1A)

Monazite forms small crystals (ca. 10 μm) with no particular zonation. They are found both included within grains and at grain boundaries of the main rock-forming minerals (quartz, biotite, plagioclase, garnet). Nine analyses were performed on six monazite grains. Among the dataset, 6 analyses define a discordia line (MSWD = 0.05; *N* = 6) with an upper intercept at 2005 ± 31 Ma and a lower intercept close to zero (530 ± 500 Ma). Other three analyses plot slightly to the right of this discordia and provide dates in the range 2032–2034 Ma. The concordance degree of ca. 97% allows to calculate a $^{207}Pb/^{206}Pb$ weighted mean age of 2034 ± 18 Ma (MSWD = 0.02) (Fig. 12e).

5.4.5 Garnet–staurolite-bearing micaschist (KOU7)

Monazite occurs as small crystals (ca. 10 μm) with no particular zoning. Similarly to sample MAD1A, they are found both included within grains and at grain boundaries of the main rock-forming minerals (quartz, biotite, plagioclase, garnet, staurolite). Eleven analyses were performed on ten grains. Ten analyses are aligned along a discordia that displays an upper intercept age of 2004 ± 16 Ma (MSWD = 0.17), which is the same within errors as the $^{207}Pb/^{206}Pb$ weighted mean age of the nine concordant to slightly discordant analyses (2002 ± 10 Ma, MSWD = 0.04; *N* = 9). The latter is adopted as our best estimate for the age of monazite in the micaschist KOU7. One analysis is significantly younger and plots concordantly at 1948 ± 33 Ma (Table S2, see Supplementary Materials, Fig. 12f).

6 Discussion

6.1 Tectono-metamorphic synthesis

The thermobarometric results from the SASCA domain suggest that peak metamorphic conditions correspond to granulite facies at the lowest structural level exposed (GDB8 and SP3B) and to amphibolite facies at the higher structural level (SAN, MAD1A and KOU7) (Figs. 13 and 14). The partially melted garnet–cordierite–sillimanite migmatitic paragneiss of Grand-Béréby (GDB8) records a prograde metamorphism that peaks in the granulite facies (~ 10 kbar, 820 °C), followed by decompression to ~ 6 kbar, and cooling. The migmatitic grey gneiss of San Pedro (SP3B) recorded a slightly lower-temperature granulite-facies metamorphic peak at ~ 8–9 kbar, 650–700 °C. The evolution of the samples SAN, MAD1A and KOU7 is in the amphibolite facies. The garnet–staurolite-bearing micaschist of Kounoukou shows a prograde evolution with a metamorphic peak at ~ 6.6 kbar, 620 °C. The P–T evolution of the garnet–sillimanite–cordierite micaschist of Madie (MAD1A) is dominated by decompression from ~ 620–650 °C, 7–8 kbar to 620–690 °C, 5–6 kbar. The staurolite-bearing micaschist of San Pedro (SAN) equilibrated at ~ 570 °C, ~ 4 kbar possibly following decompression.

The prograde evolution identified in the garnet–cordierite–sillimanite migmatitic paragneiss of Grand-Béréby (GDB8) corresponds to a burial down to ca. 38 km depth along an apparent geothermal gradient of 25–30 °C/km. The prograde evolution of the garnet–staurolite-bearing micaschist of Kounoukou points to a burial down to ca. 20 km along a similar apparent geothermal gradient of 25 °C/km. Following decompression, most P–T paths align along an apparent geothermal gradient of 40 °C/km. Such metamorphic gradients and clockwise P–T paths are typical of Barrovian-type metamorphism characterizing collisional tectonics (Miyashiro, 1961) and thickening of the Earth's crust as already proposed for the Eburnean orogenic belt (Milési *et al.*, 1992; Allibone *et al.*, 2002; Feybesse *et al.*, 2006). However, the samples presented in this paper indicate that the SASCA domain is marked by a juxtaposition of rocks with contrasting peak P–T conditions that do not depict a single regular metamorphic gradient (Fig. 13). The contrasting P–T conditions and the structural record of the SASCA domain are best explained by syncompressional crustal-scale folding, and vertical extrusion of lower-crustal material, such a proposed for example for the European Variscan belt (*e.g.*, Schulmann *et al.*, 2008; Štípská *et al.*, 2012; Krýza *et al.*, 2022). On the other hand, the moderately plunging L_2 lineation, and axes of F_2 folds, with steep axial planar surfaces parallel to regional shear zones, are compatible with a transpressional regime marked by lateral flow (*e.g.*, Lin *et al.*, 1998) typical for hot orogens (*e.g.*, Vanderhaeghe and Teyssier, 2001; Cagnard *et al.*, 2006, 2007; Vanderhaeghe *et al.*, 2020). Alternatively, the structural and metamorphic pattern of the SASCA domain might also result from the development of convective and/or diapiric gravitational instabilities as proposed for the Aegean domain (*e.g.*, Vanderhaeghe *et al.*, 2018; Louis-Napoléon *et al.*, 2020, 2021).

6.2 Chronology of tectono-metamorphic events

The ages obtained on the monazites of different samples reveal four groups: (1) oldest ages of ca. 2626, 2527 and 2439 Ma only obtained on one monazite grain from the migmatitic grey gneiss of San Pedro (SP3B); (2) ages of ca. 2037 Ma (MAD1A, SP3B, GDB8); (3) ages of ca. 2000 Ma (SP3B, GDB8, MAD1A, KOU7) and (4) very young ages of ca. 1978, 1949 and 1913 Ma (SAN, KOU7) (Figs. 12 and 13).

The ages of 2626, 2527 and 2439 Ma are attributed to the preservation of an Archean/Early Paleoproterozoic component in the protolith of the migmatitic grey gneiss of San Pedro (SP3B). These results alone do not allow to identify whether this component corresponds to an inherited grain or if it was

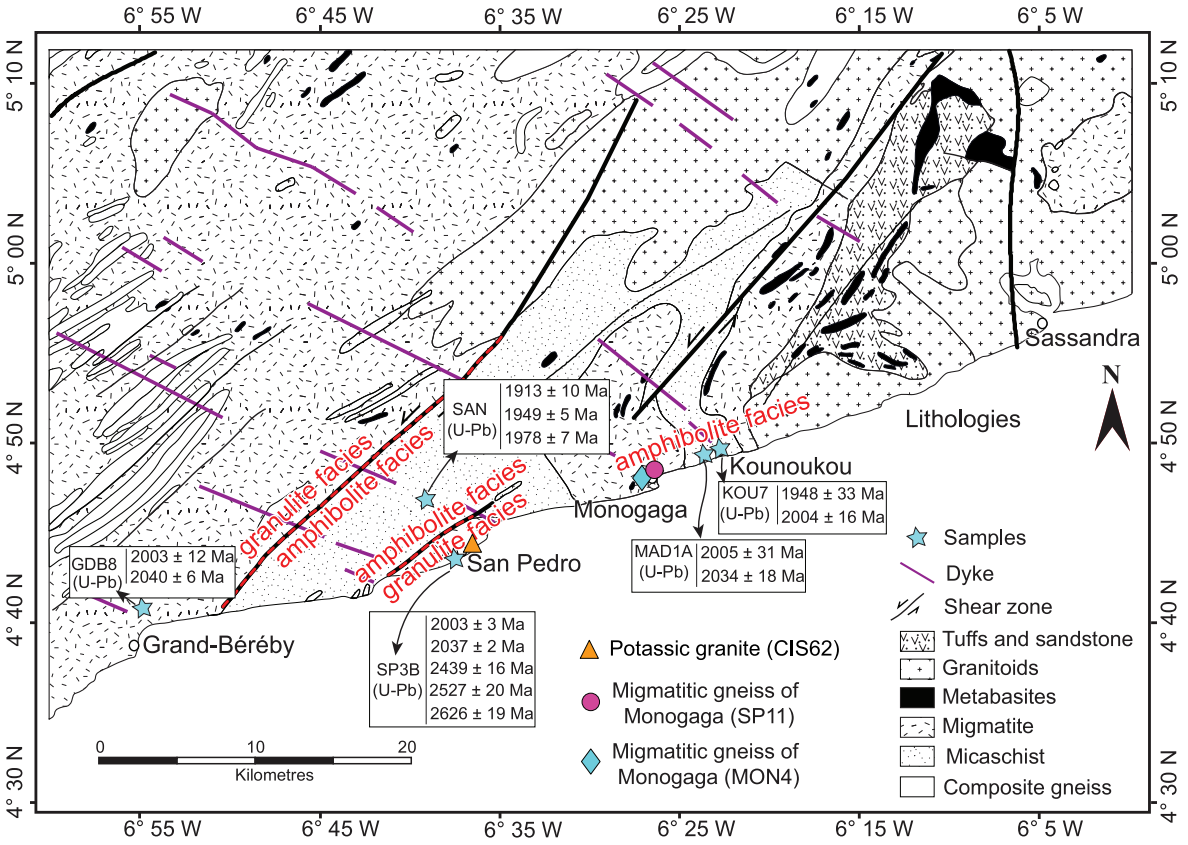

Fig. 13. Map of the SASCA domain, SW of Côte d'Ivoire, modified after Papon (1973), showing the position and the monazite age of the different samples studied (blue stars). Granulite and amphibolite facies represent the peak conditions of the corresponding areas. Migmatitic gneisses of Monogaga (MON4 and SP11) and potassic granite of San Pedro (CIS62) are from Koffi *et al.* (2022).

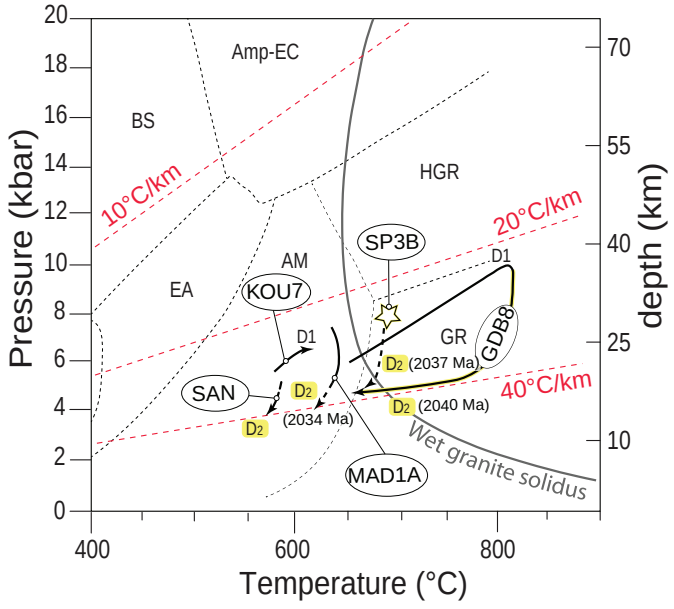

Fig. 14. Synthesis of the P–T conditions of the different rocks studied as well as their P–T path according to metamorphic facies and geothermal gradients (modified after Ernst and Liou, 2008). Abbreviations of metamorphic facies: AM: amphibolite; Amp-EC: amphibolite-eclogite; BS: blueschist; EA: epidote amphibolite; GR: sillimanite-granulite; GS: greenschist; HGR: kyanite-granulite.

part of an Archean relictual magmatic-metamorphic mineral assemblage. We note, however, that zircons from the same sample (SP3B) yield only Archean ages, and no Paleoproterozoic component was detected in the zircon population (Koffi *et al.*, 2022). The maximum temperature reached by the sample SP3B (~ 700 °C) is below the nominal closure temperature for Pb in monazite (Copeland *et al.*, 1988; Cherniak *et al.*, 2004) and preservation of relict monazite with ages older than the Paleoproterozoic is thus not surprising. This is also in agreement with numerous studies that have demonstrated the robustness and complexity of this mineral, which can survive high grade metamorphic conditions in excess of 800 °C (*e.g.*, Rubatto *et al.*, 2001; Bosch *et al.*, 2002; Kelsey *et al.*, 2008; Kelsey and Powell, 2011; Yakymchuk and Brown, 2014; Guergouz *et al.*, 2018). The ages of ca. 2037 Ma are interpreted as dating the Paleoproterozoic metamorphism across the region, in agreement with the position of the monazite grains in the penetrative foliation S_2 (Fig. 11b). The association of this foliation with decompression implies that this age dates the exhumation period of the rocks in the SASCA domain.

The ages of ca. 2000 Ma and younger (ca. 1978 to 1913 Ma) are generally found in monazite inclusions in andalusite, which suggests that they could be associated with decompression and cooling (Fig. 9a). These ages could result from two types of processes: (1) (partial) resetting of older crystals by either long-term cooling with periodic opening of the U–Pb system (McFarlane *et al.*, 2006;

Kirkland *et al.*, 2016) or isotopic disturbance by fluids (Teufel and Heinrich, 1997; Schmidt *et al.*, 2007; Bosse *et al.*, 2009; Williams *et al.*, 2011; Seydoux-Guillaume *et al.*, 2012; Kirkland *et al.*, 2016); (2) episodic crystallisation of monazite during the cooling period (Kirkland *et al.*, 2016; Guergouz *et al.*, 2018).

6.3 Regional correlations

Similar clockwise P–T paths with peak-pressure conditions corresponding to gradients of ~20–30 °C/km were identified elsewhere in the West African Craton (Pitra *et al.*, 2010; Ganne *et al.*, 2012; Block *et al.*, 2015; McFarlane, 2018; Kone, 2020). In the Kouibli zone of the Kenema-Man domain (Fig. 2), this P–T path is associated with similar ages of 2030–2050 Ma (Sm–Nd garnet, U–Pb monazite; Kouamelan *et al.*, 1997, 2018; Cocherie *et al.*, 1998). Similar ages (2041 ± 19 Ma and 2037 ± 14 Ma, U–Pb zircon) were also reported from southeastern Guinea and interpreted as a late high-temperature metamorphic event (Thiéblemont *et al.*, 2004). In the Kedougou Kenieba Inlier of eastern Senegal, two metamorphic phases were dated at ca. 2085 and 2050 Ma, respectively (Kone, 2020; U–Pb monazite and Sm–Nd garnet).

Elsewhere, however, the associated U–Pb monazite ages are different. They are of ca. 2135 Ma and ca. 2073 Ma in northern and southern Ghana, respectively (Block *et al.*, 2015; McFarlane *et al.*, 2019). In the Damang mine in Ghana, the minimum age for the onset of the exhumation is 2005 ± 26 Ma according to U–Th–total Pb EPMA analyses of metamorphic monazite grains (White *et al.*, 2014). In the same study area, ages ranging from 1980 ± 9 Ma to 1898 ± 11 Ma were obtained by the $^{40}Ar/^{39}Ar$ biotite method and attributed to a protracted period of slow cooling (White *et al.*, 2014).

The youngest U–Pb monazite ages obtained in this study (ca. 2000, 1978–1913 Ma) were not previously reported in the literature of the West African Craton. In the study area, they are localized in some samples only (GDB8, SAN, KOU7 in Fig. 15). At the same time, they are the only ages found in one of the samples (SAN), where older ages (ca. 2037 Ma) are completely absent. This suggests a dissolution-precipitation of monazite in connection with fluid circulations associated with late reactivation of some of the transcurrent shear zones, consistent with the localized distribution of this overprint.

In South America, metamorphic monazite ages obtained by several methods (U–Pb TIMS, LA-SF-ICPMS, EPMA, SHRIMP, TIMS and Pb–Pb TIMS) show that these Paleoproterozoic terrains were affected by a long metamorphic period in the range from ca. 2100 to 1920 Ma (Machado *et al.*, 1992; Schrank and Machado, 1996; Silva *et al.*, 1996; Noce *et al.*, 1998; Barbosa *et al.*, 2000, 2004; Delor *et al.*, 2003; Vlach *et al.*, 2003; da Rosa-Costa *et al.*, 2008; Fraga *et al.*, 2008, 2009, 2017; Leite *et al.*, 2009; De Roever *et al.*, 2015; Kroonenberg *et al.*, 2016; Medeiros Júnior *et al.*, 2016; Aguilar *et al.*, 2017; Cutts *et al.*, 2018). Similar to the SASCA region, in the northern part of Guiana Shield the dominant deformation D_2 is associated with major sinistral strike-slip faults (Vanderhaeghe *et al.*, 1998; Delor *et al.*, 2003). The very young metamorphic ages obtained on monazites (< 2000 Ma) in the São Francisco Craton characterize a long period of slow cooling (1 °C/Ma) down to ca. 1940 Ma (Aguilar *et al.*, 2017) (Fig. 15f). Similarly, high-grade metamorphism is dated at 2046 ± 6 Ma in the Borborema Province, north of the São Francisco Craton (Calado *et al.*, 2019). The south of the São Francisco Craton as well as the Guiana Shield are characterized by a long-lived metamorphism at ca. 2100–1940 Ma including a syn-collisional period of ca. 2100–2070 Ma (Peucat *et al.*, 2011; Aguilar *et al.*, 2017; Fraga and Cordani, 2019). da Rosa-Costa *et al.* (2008) found very similar results for the late orogenic stage of the collisional orogeny along the Amapá Block. The similarity in the metamorphic age spans suggests a potential link between the southern WAC and South America at the time of the Eburnean Orogeny as proposed by Onstott and Hargraves (1981), Ledru *et al.* (1994), Nomade *et al.* (2003) and Traoré *et al.* (2022).

6.4 Geodynamic implications for Archean and Paleoproterozoic orogenic processes

We have documented a polyphased tectono-metamorphic evolution of the metasediments and migmatitic gneisses in the SASCA domain. The reconstructed P–T–t–d paths imply thickening of the crust under moderate apparent geothermal gradients of 20–30 °C/km and maximum burial depth of 20–30 km recorded in the granulite facies samples SP3B and GDB8 and 15–25 km in the samples KOU7 and MAD1A (Fig. 14). This is consistent with burial of supracrustal rocks represented mostly by sediments and volcanics in a collisional setting. The initial burial corresponding to the deformation phase D_1 operated prior to ca. 2037 Ma (which is the age of D_2). Additionally, a sample of Archean migmatitic gneiss, from the vicinity of Monogaga (sample SP11 in Fig. 13), reveals ~2070 Ma metamorphic overprint documented by younger zircon rims (Koffi *et al.*, 2022).

The metamorphic pressure peak is first followed by a nearly isothermal decompression, interpreted as rapid exhumation, and then by simultaneous decompression and cooling. We note that the ca. 2037 Ma old monazites are predominantly found in samples GDB8, SP3B and MAD1A, which record a retrograde path under amphibolite-facies conditions (MAD1A and GDB8) and that are pervasively affected by the NE-SW trending S_2 foliation. Therefore, we suggest that the ca. 2037 Ma ages date the retrograde phase D_2.

The monazite metamorphic ages corroborate the conclusion of Kouamelan *et al.* (1997) and Pitra *et al.* (2010) from the Kouibli area that the major tectono-metamorphic polyphased event is related to the Eburnean orogeny. The presence of relictual Archean zircon and monazite grains is consistent with the interpretation of the SASCA domain as a so-called "metacraton" (Abdelsalam *et al.*, 2002; Liégeois *et al.*, 2005), which suggests tectonic accretion of Paleoproterozoic and Archean domains affected by metamorphism and deformation during the Eburnean orogeny. Nevertheless, this does not preclude the hypothesis of a sedimentary protolith containing detrital zircon grains.

In the Kouibli area to the N of the study zone, the mechanism of homogeneous shortening accommodated by a combination of shear zones and lateral crustal spreading (Cagnard *et al.*, 2006, 2007; Cruden *et al.*, 2006; Rey and Houseman, 2006) was suggested by Pitra *et al.* (2010) based on the absence of large-scale thrust systems. Nevertheless,

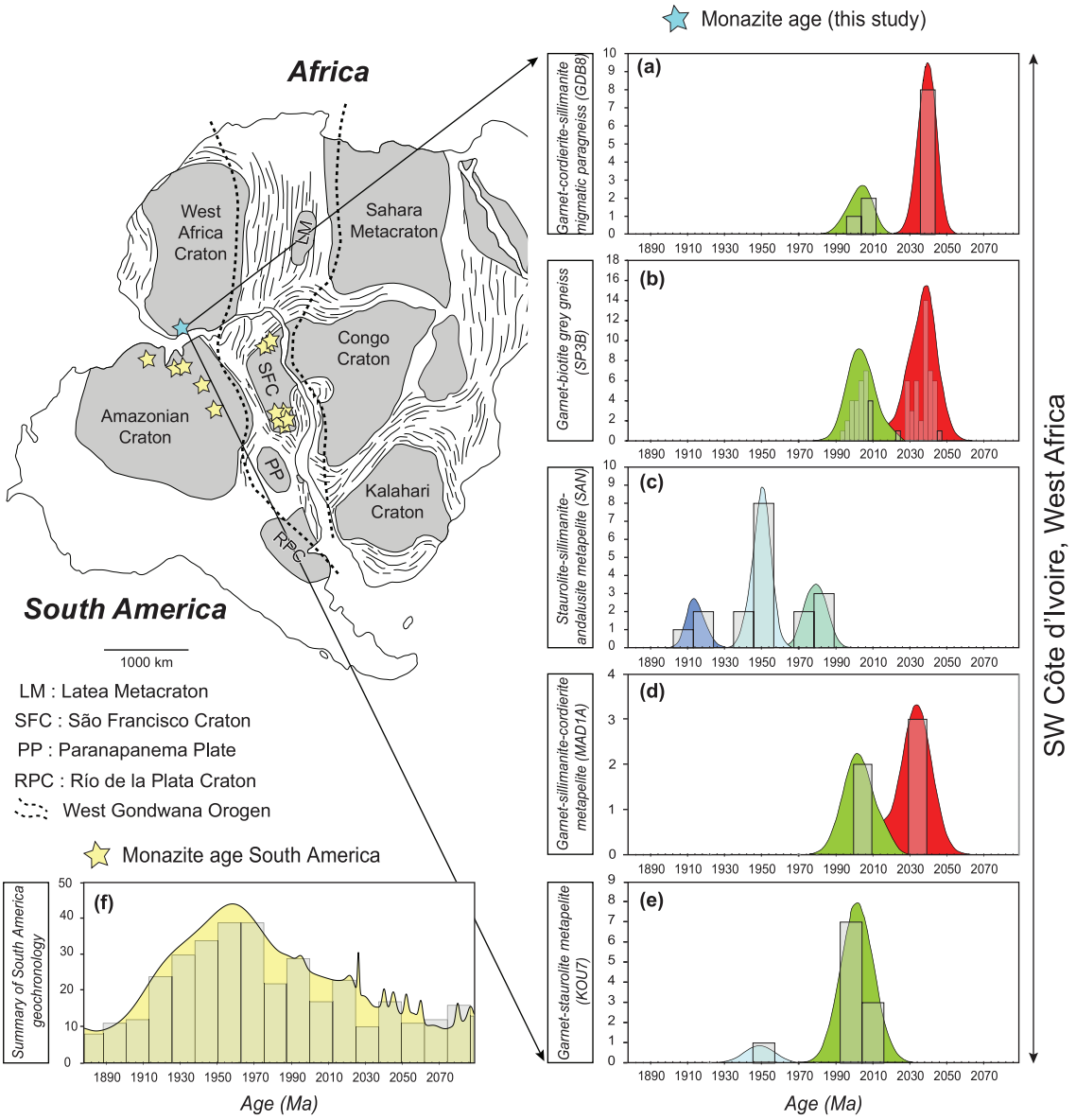

Fig. 15. Relative probability plots of U–Pb monazite ages obtained in this study (a–e) and U–Pb monazite data obtained in South America (f) (Machado *et al.*, 1992; Schrank and Machado, 1996; Silva *et al.*, 1996; Noce *et al.*, 1998; Barbosa *et al.*, 2000, 2004; Vlach *et al.*, 2003; da Rosa-Costa *et al.*, 2008; Fraga *et al.*, 2008, 2009; Leite *et al.*, 2009; Medeiros Júnior *et al.*, 2016; Aguilar *et al.*, 2017; Cutts *et al.*, 2018).

metamorphic and structural mapping of the SASCA area (Fig. 13) shows the juxtaposition of rocks with contrasted metamorphic facies from amphibolite to granulite facies between the zones of Grand-Béréby, Kounoukou and San Pedro. The domains with different metamorphic conditions seem to be delimited by transcurrent shear zones except between SP3B and MAD1A/KOU7. The model (Fig. 16) shows tectonic juxtaposition of units with different peak P–T conditions implying metamorphism at different crustal levels. The character of the P–T–t paths suggests that the tectonic juxtaposition of amphibolite and granulite facies rocks would occur during their exhumation after reaching the peak P–T conditions. Flat-lying thrust zones were not found in the field. Either they were never present or they were transposed into steep foliations and folds during later stages of the Eburnean orogeny. To explain the total vertical displacement between the units, which is in the order of 6–10 km, we advocate large-scale crustal folding (Schulmann *et al.*, 2008; Štípská *et al.*, 2012) and/or gravitational convective-diapiric instabilities (Vanderhaeghe *et al.*, 2018) associated with lateral crustal flow and accompanied by transcurrent subvertical NE-SW trending shear zones during the D_2 phase, now defining the structural grain of the whole area.

Collisional setting during the assembly of the Archean and Paleoproterozoic terrains of the WAC was evoked in the work of Camil (1981, 1984), Camil *et al.* (1983), Triboulet and Feybesse (1998), Thiéblemont *et al.* (2004), Pitra *et al.* (2010), in western Côte d'Ivoire, Liberia and Sierra Leone and in the work of Eglinger *et al.* (2017) in Central Guinea. Many works suggest that Paleoproterozoic formations were deformed in a

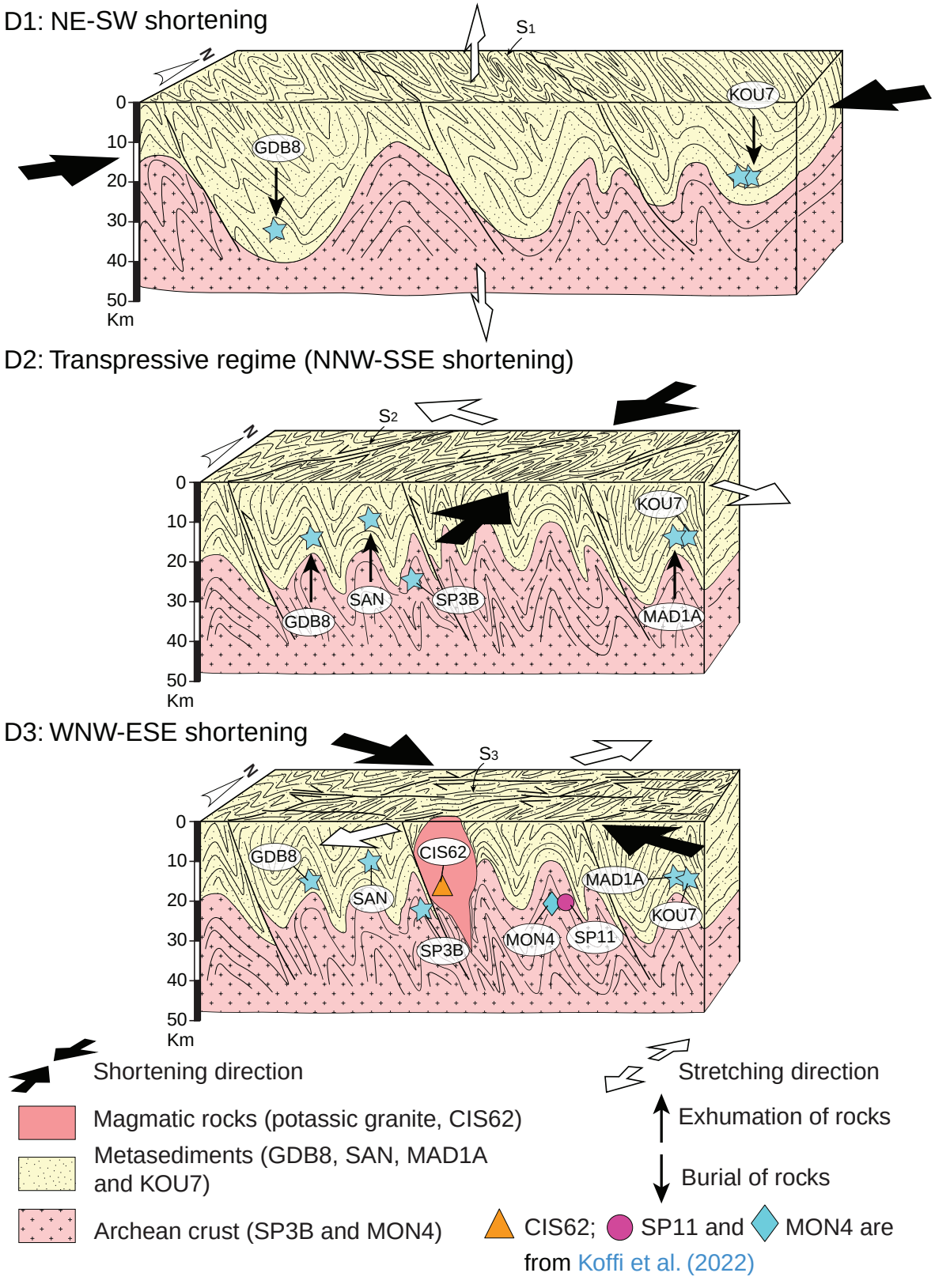

Fig. 16. An evolutionary sketch showing the exhumation of rocks in SW Côte d'Ivoire. CIS62: potassic granite of San Pedro; MON4 and SP11: migmatitic gneisses of Monogaga (Koffi *et al.*, 2022).

transpressive context in the late stages of the Eburnean orogeny (Ledru *et al.*, 1991; Feybesse *et al.*, 2006; Baratoux *et al.*, 2011; Jessell *et al.*, 2012; Chardon *et al.*, 2020). However, the proposed exhumation mechanisms of the rocks differ from one area to another. In NW Ghana, the exhumation of the lower crust is attributed to a N-S extension during the gravitational collapse generating anatectic domes (Block *et al.*, 2015). In SW Ghana, the work of McFarlane *et al.* (2019) describes a transtensional ENE-WSW regime for the exhumation of the middle and lower crust. Neither ductile normal faults similar to the ones described in NW Ghana, nor folds with shallow-plunging fold axes oblique to the orientation of the major shear zones similar to those in SW Ghana, were found in our study area. Therefore, we conclude that the extensional component of deformation during exhumation was either negligible or its record was overprinted by the later intense transpressive deformation. Our study confirms the diversity of metamorphic gradients in the West African Craton documented by several recent studies (Ganne *et al.*, 2012; Block *et al.*, 2015; McFarlane *et al.*, 2019). In some areas, such as Burkina Faso and Ghana, the studied metamorphic rocks recorded an apparent cold geothermal gradient of ~ 15 °C/km (Ganne *et al.*, 2012; Block *et al.*, 2015); however, in SW Côte d'Ivoire such cold gradients were not found.

In the framework of the ongoing discussion about the character of the orogenic processes at the Archean-Paleoproterozoic transition, P–T conditions combined with (micro)structural observations and geochronology presented in this paper suggest a predominance of diffuse crustal thickening owing to tectonic forces followed by and partly concomitant with gravity-driven lateral flow of the thickened crust. The final stages of the Eburnean orogeny in the SASCA domain might be compared to the orogenic plateau stage of modern orogenic belts as described in Bajolet *et al.* (2015) or in Vanderhaeghe (2009, 2012).

7 Conclusion

The SASCA domain in SW Côte d'Ivoire is characterized by the tectonic juxtaposition of granulite-facies migmatitic paragneiss with amphibolite-facies migmatitic grey gneiss and micaschists. The metamorphic conditions recorded in these rocks show a Barrovian-type metamorphism. Granulite-facies rocks reached a syn-D_1 metamorphic peak of 10 kbar at 820 °C followed by a retrograde evolution marked by decompression and by cooling. This is consistent with a burial down to 38 km depth before exhumation. For the amphibolite-facies rocks, the syn-D_1 prograde evolution (garnet–staurolite-bearing micaschist at Kounoukou with a metamorphic peak at ca. 6.6 kbar, 620 °C) reveals a burial down to 25 km along an apparent geothermal gradient of ~ 25 °C/km. During subsequent exhumation these high- and medium-grade rocks reached an apparent geothermal gradient of ~ 40 °C/km. This metamorphic phase was associated with the development of the dominant foliation S_2 at ca. 2037 Ma. The exhumation results from a combination of crustal-scale folding and/or convective-diapiric instabilities associated with lateral flow owing to a regional transcurrent regime, which would explain the juxtaposition of rocks that reached significantly different P–T conditions.

Very young monazites (ca. 2000 Ma and 1978 to 1913 Ma) found in all dated samples crystallized during the retrograde path and could result from two types of processes: (1) (partial) resetting of older crystals by either long-term cooling with periodic opening of the U–Pb system or isotopic disturbance by fluids, or (2) episodic crystallization of monazite during the cooling period. This is the very first study in the WAC, which determines such young metamorphic ages allowing a correlation with the Guiana Shield where these ages are more abundant.

Supplementary Material

Table S1: LA-ICP-MS U-Pb analyses for standard material Managotry and Moacyr.
Table S2: LA-ICP-MS U-Pb data for monazites from the studied samples.

Table S3: Summary of monazite ages from South America.

The Supplementary Material is available at http://www.bsgf.fr/10.1051/bsgf/2023007/olm.

Acknowledgements. This project is part of a PhD study of A.Y. Koffi, partially funded by the T2GEM project (Geophysical and Geochemical Technologies for Mineral Exploration) and by the project "West African Exploration Initiative" (WAXI). We wish to gratefully acknowledge AMIRA International and the industry sponsors for their support of the WAXI project (P934B). We are also appreciative of the contribution of the various geological surveys and departments of mines in West Africa as sponsors in kind of WAXI. We would like to thank the scholarship directorate of the Ministry of Higher Education and Scientific Research of Côte d'Ivoire for awarding A.Y.K. a scholarship for a doctoral internship in France to carry out the analyses. The African Network of Institutions in Earth Sciences (ANESI) for the financing of the stay of A.Y.K. in Senegal to improve the quality of this work. The authors acknowledge the French National Research Institute for Sustainable Development (IRD, LMI MINERWA Laboratory for Responsible Mining in West Africa) for funding a part of this research project. We are grateful to P. de Parseval. S. Gouy and T. Agouy for their help in acquiring microanalysis and F. Barrère de Parseval for the thin sections. The authors gratefully acknowledge Lêda Maria Fraga and one anonymous reviewer for their constructive reviews.

References

Abdelsalam MG, Liégeois J-P, Stern RJ. 2002. The Saharan Metacraton. *Journal of African Earth Sciences* 34: 119–136.

Aguilar C, Alkmim FF, Lana C, Farina F. 2017. Palaeoproterozoic assembly of the São Francisco Craton, SE Brazil: New insights from U–Pb titanite and monazite dating. *Precambrian Research* 289: 95–115.

Allibone A, Teasdale J, Cameron G, Etheridge M, Uttley P, Soboh A, *et al.* 2002. Timing and structural controls on gold mineralization at the Bogoso Gold Mine, Ghana, West Africa. *Economic Geology* 97: 949–969. https://doi.org/10.2113/gsecongeo.97.5.949.

Auvray B, Peucat J-J, Potrel A, Burg J-P, Caruba C, Dars R, *et al.* 1992. Données géochronologiques nouvelles sur l'Archéen de l'Amsaga (Dorsale Réguibat, Mauritanie). Paris : Gauthier-Villars.

Bajolet F, Chardon D, Martinod J, Gapais D, Kermarrec J-J. 2015. Synconvergence flow inside and at the margin of orogenic plateaus: Lithospheric-scale experimental approach. *Journal of Geophysical Research: Solid Earth* 120: 6634–6657.

Baratoux L, Metelka V, Naba S, Jessell MW, Grégoire M, Ganne J. 2011. Juvenile Paleoproterozoic crust evolution during the Eburnean orogeny (~ 2.2–2.0 Ga), western Burkina Faso. *Precambrian Research* 191: 18–45.

Barbosa JSF, Martin H, Peucat JJ. 2000. Archean *vs.* Paleoproterozoic crustal evolution of the Laje, Mutuipe, Brejões and Santa Inês Region, Jequié Complex, Bahia, Brazil. In: *31st International Geological Congress, Rio de Janeiro, Brazil, CD-ROM (2000)* (Vol. 31).

Barbosa J, Martin H, Peucat J-J. 2004. Palaeoproterozoic dome-forming structures related to granulite-facies metamorphism, Jequié block, Bahia, Brazil: Petrogenetic approaches. *Precambrian Research* 135: 105–131.

Bédard JH. 2006. A catalytic delamination-driven model for coupled genesis of Archaean crust and sub-continental lithospheric mantle. *Geochimica et Cosmochimica Acta* 70: 1188–1214.

Begg GC, Griffin WL, Natapov LM, O'Reilly SY, Grand SP, O'Neill CJ, *et al.* 2009. The lithospheric architecture of Africa: Seismic tomography, mantle petrology, and tectonic evolution. *Geosphere* 5: 23–50. https://doi.org/10.1130/GES00179.1.

Berger J, Diot H, Lo K, Ohnenstetter D, Féménias O, Pivin M, *et al.* 2013. Petrogenesis of Archean PGM-bearing chromitites and associated ultramafic-mafic-anorthositic rocks from the Guelb el Azib layered complex (West African Craton, Mauritania). *Precambrian Research* 224: 612–628.

Bessoles B. 1977. Géologie de l'Afrique. Le Craton Ouest Africain. *Memoire du BRGM* 88: 402.

Block S, Ganne J, Baratoux L, Zeh A, Parra-Avila LA, Jessell M, *et al.* 2015. Petrological and geochronological constraints on lower crust exhumation during Paleoproterozoic (Eburnean) orogeny, NW Ghana, West African Craton. *Journal of Metamorphic Geology*, John Wiley & Sons, Ltd 33: 463–494.

Block S, Baratoux L, Zeh A, Laurent O, Bruguier O, Jessell M, *et al.* 2016. Paleoproterozoic juvenile crust formation and stabilisation in the southeastern West African Craton (Ghana): New insights from U–Pb–Hf zircon data and geochemistry. *Precambrian Research*, Elsevier 287: 1–30.

Boher M, Abouchami W, Michard A, Albarede F, Arndt NT. 1992. Crustal growth in West Africa at 2.1 Ga. *Journal of Geophysical Research: Solid Earth* 97: 345–369.

Bonzi WM-E, Vanderhaeghe O, Van Lichtervelde M, Wenmenga U, André-Mayer A-S, Salvi S, *et al.* 2021. Petrogenetic links between rare metal-bearing pegmatites and TTG gneisses in the West African Craton: The Mangodara district of SW Burkina Faso. *Precambrian Research* 364: 106359.

Bosch D, Hammor D, Bruguier O, Caby R, Luck J-M. 2002. Monazite "*in situ*" $^{207}Pb/^{206}Pb$ geochronology using a small geometry high-resolution ion probe. Application to Archaean and Proterozoic rocks. *Chemical Geology* 184: 151–165.

Bosch D, Garrido CJ, Bruguier O, Dhuime B, Bodinier J-L, Padrón-Navarta JA, *et al.* 2011. Building an island-arc crustal section: Time constraints from a LA-ICP-MS zircon study. *Earth and Planetary Science Letters* 309: 268–279.

Bosse V, Boulvais P, Gautier P, Tiepolo M, Ruffet G, Devidal JL, *et al.* 2009. Fluid-induced disturbance of the monazite Th–Pb chronometer: *In situ* dating and element mapping in pegmatites from the Rhodope (Greece, Bulgaria). *Chemical Geology* 261: 286–302.

Bourges F, Debat P, Tollon F, Munoz M, Ingles J. 1998. The geology of the Taparko gold deposit, Birimian greenstone belt, Burkina Faso, West Africa. *Mineralium Deposita* 33: 591–605.

Brown M. 2014. The contribution of metamorphic petrology to understanding lithosphere evolution and geodynamics. *Geoscience Frontiers* 5: 553–569.

Brown M, Johnson T, Gardiner NJ. 2020. Plate tectonics and the Archean Earth. *Annual Review of Earth and Planetary Sciences* 48: 291–320.

Bruguier O, Hammor D, Bosch D, Caby R. 2009. Miocene incorporation of peridotite into the Hercynian basement of the Maghrebides (Edough massif, NE Algeria): Implications for the geodynamic evolution of the Western Mediterranean. *Chemical Geology* 261: 172–184.

Caby R, Delor C, Agoh O. 2000. Lithologie, structure et métamorphisme des formations birimiennes dans la région d'Odienné (Côte d'Ivoire) : rôle majeur du diapirisme des plutons et des décrochements en bordure du Craton de Man. *Journal of African Earth Sciences*, Elsevier 30: 351–374.

Cagnard F, Durrieu N, Gapais D, Brun J-P, Ehlers C. 2006. Crustal thickening and lateral flow during compression of hot lithospheres, with particular reference to Precambrian times. *Terra Nova* 18: 72–78.

Cagnard F, Gapais D, Barbey P. 2007. Collision tectonics involving juvenile crust: The example of the southern Finnish Svecofennides. *Precambrian Research* 154: 125–141.

Calado B de O, Costa FG, Gomes IP, Rodrigues JB. 2019. Evidence for ca. 2046 Ma high-grade metamorphism in Paleoproterozoic metasedimentary rocks of the northern Borborema Province, NE Brazil: Constraints from U–Pb (LA-ICP-MS) zircon ages. *Journal of the Geological Survey of Brazil* 2: 137–150.

Camil J. 1981. Un exemple de métamorphisme prograde de la base du faciès des amphibolites au faciès des granulites dans la région de Man (Ouest de la Côte d'Ivoire). *C. R. Acad. Sci. Paris* 93: 513–518.

Camil J. 1984. Pétrographie, chronologie des ensembles granulitiques archéens et formations associées de la région de Man (Côte d'Ivoire) : implication pour l'histoire géologique du Craton Ouest-Africain. PhD Thesis, Université Félix Houphouët-Boigny, Abidjan, 306 p.

Camil J, Tempier P, Pin C. 1983. Âge Libérien des quartzites a magnétite de la région de Man (Côte d'Ivoire) et leur place dans l'orogène Libérien. *C. R. Acad. Sci. Paris* 296: 149–151.

Cawood PA, Hawkesworth CJ, Dhuime B. 2013. The continental record and the generation of continental crust. *GSA Bulletin*, GeoScienceWorld 125: 14–32.

Chardon D, Bamba O, Traoré K. 2020. Eburnean deformation pattern of Burkina Faso and the tectonic significance of shear zones in the West African Craton. *Bulletin de la Société Géologique de France* 191: 2.

Cherniak DJ, Watson EB, Grove M, Harrison TM. 2004. Pb diffusion in monazite: A combined RBS/SIMS study[1] ([1]Associate editor: Y. Amelin). *Geochimica et Cosmochimica Acta* 68: 829–840.

Cocherie A, Legendre O, Peucat JJ, Kouamelan AN. 1998. Geochronology of polygenetic monazites constrained by *in situ* electron microprobe Th–U–total lead determination: Implications for lead behaviour in monazite. *Geochimica et Cosmochimica Acta* 62: 2475–2497.

Coggon R, Holland TJB. 2002. Mixing properties of phengitic micas and revised garnet-phengite thermobarometers. *Journal of Metamorphic Geology* 20: 683–696.

Condie KC. 1994. Archean crustal evolution. Amsterdam: Elsevier, 528 p.
Condie KC. 2018. A planet in transition: The onset of plate tectonics on Earth between 3 and 2 Ga? *Geoscience Frontiers* 9: 51–60.
Copeland P, Parrish RR, Harrison TM. 1988. Identification of inherited radiogenic Pb in monazite and its implications for U–Pb systematics. *Nature*, Nature Publishing Group 333: 760–763.
Cruden AR, Nasseri MHB, Pysklywec R. 2006. Surface topography and internal strain variation in wide hot orogens from three-dimensional analogue and two-dimensional numerical vice models. *Geological Society, London, Special Publications*, The Geological Society of London 253: 79–104.
Cutts K, Lana C, Alkmim F, Peres GG. 2018. Metamorphic imprints on units of the southern Araçuaí belt, SE Brazil: The history of superimposed Transamazonian and Brasiliano orogenesis. *Gondwana Research* 58: 211–234.
da Rosa-Costa LT, Lafon J-M, Cocherie A, Delor C. 2008. Electron microprobe U–Th–Pb monazite dating of the Transamazonian metamorphic overprint on Archean rocks from the Amapá Block, southeastern Guiana Shield, northern Brazil. *Journal of South American Earth Sciences* 26: 445–462.
de Capitani C, Brown TH. 1987. The computation of chemical equilibrium in complex systems containing non-ideal solutions. *Geochimica et Cosmochimica Acta* 51: 2639–2652.
de Capitani C, Petrakakis K. 2010. The computation of equilibrium assemblage diagrams with Theriak/Domino software. *American Mineralogist* 95: 1006–1016.
De Roever EW, Lafon JM, Delor C, Cocherie A, Guerrot C. 2015. Orosirian magmatism and metamorphism in Suriname: New geochronological constraints. *Contribuiç oes a Geologia da Amazônia* 9: 359–372.
De Waele B, Lacorde M, Vergara F, Chan G. 2015. New insights on proterozoic tectonics and sedimentation along the peri-Gondwanan West African margin based on zircon U–Pb SHRIMP geochronology. *Precambrian Research* 259: 156–175.
de Wit MJ. 1998. On Archean granites, greenstones, cratons and tectonics: Does the evidence demand a verdict? *Precambrian Research* 91: 181–226.
Debat P, Nikiéma S, Mercier A, Lompo M, Béziat D, Bourges F, *et al.* 2003. A new metamorphic constraint for the Eburnean orogeny from Paleoproterozoic formations of the Man Shield (Aribinda and Tampelga countries, Burkina Faso). *Precambrian Research* 123: 47–65. https://doi.org/10.1016/S0301-9268(03)00046-9.
Delor C, Siméon Y, Vidal M. 1995. Peri-plutonic gravity driven deformations and transcurrent tectonics between 2.2 and 2.1 By: A case study from the Birimian Cycle in Ivory Coast. *EUG* 102.
Delor C, Lahondère D, Egal E, Lafon J-M, Cocherie A, Guerrot C, *et al.* 2003. Transamazonian crustal growth and reworking as revealed by the 1:500 000-scale geological map of French Guiana. *Géologie de la France* 2-4: 5–57.
Diallo M, Bouabdellah M, Levresse G, Yans J, Castorina F, Klugel A, *et al.* 2021. Mineralogy, fluid inclusion, and C–O–Sr isotope geochemistry to unravel the evolution of the magmatic-hydrothermal system at the Igoudrane Silver-rich deposit (Imiter District, Eastern Anti-Atlas, Morocco). *Minerals* 11. https://doi.org/10.3390/min11090997.
Doumbia S, Pouclet A, Kouamelan A, Peucat JJ, Vidal M, Delor C. 1998. Petrogenesis of juvenile-type Birimian (Paleoproterozoic) granitoids in Central Côte-d'Ivoire, West Africa: Geochemistry and geochronology. *Precambrian Research* 87: 33–63.
Eglinger A, Thébaud N, Zeh A, Davis J, Miller J, Parra-Avila LA, *et al.* 2017. New insights into the crustal growth of the Paleoproterozoic margin of the Archean Kéména-Man domain, West African Craton (Guinea): Implications for gold mineral system. *Precambrian Research* 292: 258–289.
Ennih N, Liégeois J-P. 2008. The boundaries of the West African Craton, with special reference to the basement of the Moroccan metacratonic Anti-Atlas belt. *Geological Society, London, Special Publications* 297: 1–17.
Ernst WG, Liou JG. 2008. High- and ultrahigh-pressure metamorphism: Past results and future prospects. *American Mineralogist* 93: 1771–1786.
Fabre R. 1995. Évolution géodynamique des terrains d'un proterozoïque inférieur (birimien) dans le centre de la Côte d'Ivoire (Afrique de l'Ouest) : une mise au point. Thèse de doctorat, Habilitation à Diriger des Recherches, Université de Bordeaux, France, 422 p.
Feybesse J-L, Milési J-P. 1994. The Archaean/Proterozoic contact zone in West Africa: A mountain belt of décollement thrusting and folding on a continental margin related to 2.1 Ga convergence of Archaean cratons? *Precambrian Research* 69: 199–227.
Feybesse J-L, Milesi J-P, Ouedraogo MF, Prost A. 1990. La ceinture protérozoïque inférieur de Boromo-Goren (Burkina Faso) : un exemple d'interférence entre deux phases transcurrentes éburnéennes. Paris : Gauthier-Villars, pp. 1353–1360.
Feybesse J-L, Billa M, Guerrot C, Duguey E, Lescuyer J-L, Milesi J-P, *et al.* 2006. The paleoproterozoic Ghanaian province: Geodynamic model and ore controls, including regional stress modeling. *Precambrian Research* 149: 149–196.
Fraga LM, Cordani U. 2019. Early Orosirian tectonic evolution of the Central Guiana Shield: Insights from new U–Pb SHRIMP data. In: *11th Inter Guiana Geological Conference: Tectonics and Metallogenesis of NE South America*, pp. 59–62.
Fraga LM, Reis NJ, Dall'Agnol R, Armstrong R. 2008. Cauarane–Coeroene belt – The tectonic southern limit of the preserved rhyacian crustal domain in the Guyana Shield, northern Amazonian Craton. In: *International Geological Congress* (Vol. 33).
Fraga LMF, Reis NJ, Dall'Agnol A. 2009. Cauarane–Coeroeni belt – The main tectonic feature of the central Guyana Shield, northern Amazonian Craton. Extended abstract. In: *Simpósio de Geologia da Amazônia*, Vol. 11, Amazonas, Manaus.
Fraga LM, Cordani U, Kroonenberg S, Roever ED, Nadeau S, Maurer VC. 2017. U–Pb SHRIMP new data on the high-grade supracrustal rocks of the Cauarane–Coeroeni belt – Insights on the tectonic Eo-Orosirian evolution of the Guiana Shield. In: *Conference: Anais Do 15° Simpósio De Geologia Da Amazônia, Belém, Brasil*, pp. 486–490.
Ganne J, De Andrade V, Weinberg RF, Vidal O, Dubacq B, Kagambega N, *et al.* 2012. Modern-style plate subduction preserved in the Palaeoproterozoic West African Craton. *Nature Geoscience*, Nature Publishing Group 5: 60–65. https://doi.org/10.1038/ngeo1321.
Ganne J, Gerbault M, Block S. 2014. Thermo-mechanical modeling of lower crust exhumation – Constraints from the metamorphic record of the Palaeoproterozoic Eburnean orogeny, West African Craton. *Precambrian Research* 243: 88–109.
Gapais D, Potrel A, Machado N, Hallot E. 2005. Kinematics of long-lasting Paleoproterozoic transpression within the Thompson Nickel Belt, Manitoba, Canada. *Tectonics* 24.
Gapais D, Pelletier A, Ménot R-P, Peucat J-J. 2008. Paleoproterozoic tectonics in the Terre Adélie Craton (East Antarctica). *Precambrian Research* 162: 531–539.
Gasquet D, Barbey P, Adou M, Paquette JL. 2003. Structure, Sr-Nd isotope geochemistry and zircon U–Pb geochronology of the granitoids of the Dabakala area (Côte d'Ivoire): Evidence for a 2.3 Ga crustal growth event in the Palaeoproterozoic of West Africa? *Precambrian Research* 127: 329–354.

Guergouz C, Martin L, Vanderhaeghe O, Thébaud N, Fiorentini M. 2018. Zircon and monazite petrochronologic record of prolonged amphibolite to granulite facies metamorphism in the Ivrea-Verbano and Strona-Ceneri Zones, NW Italy. *Lithos* 308-309: 1–18.

Günther D, Heinrich CA. 1999. Comparison of the ablation behaviour of 266 nm Nd:YAG and 193 nm ArF excimer lasers for LA-ICP-MS analysis. *Journal of Analytical Atomic Spectrometry*, Royal Society of Chemistry 14: 1369–1374.

Hamilton WB. 2011. Plate tectonics began in Neoproterozoic time, and plumes from deep mantle have never operated. *Lithos* 123: 1–20.

Hirdes W, Davis DW. 2002. U–Pb Geochronology of Paleoproterozoic rocks in the southern part of the Kedougou-Kéniéba Inlier, Senegal, West Africa: Evidence for diachronous accretionary development of the Eburnean Province. *Precambrian Research* 118: 83–99.

Holland TJB, Powell R. 1998. An internally consistent thermodynamic data set for phases of petrological interest. *Journal of Metamorphic Geology* 16: 309–343.

Holland T, Powell R. 2003. Activity-composition relations for phases in petrological calculations: An asymmetric multicomponent formulation. *Contributions to Mineralogy and Petrology* 145: 492–501.

Holness MB, Cesare B, Sawyer EW. 2011. Melted rocks under the microscope: microstructures and their interpretation. *Elements* 7: 247–252.

Horstwood MSA, Foster GL, Parrish RR, Noble SR, Nowell GM. 2003. Common-Pb corrected *in situ* U–Pb accessory mineral geochronology by LA-MC-ICP-MS. *Journal of Analytical Atomic Spectrometry*, The Royal Society of Chemistry 18: 837–846.

Jessell MW, Amponsah PO, Baratoux L, Asiedu DK, Loh GK, Ganne J. 2012. Crustal-scale transcurrent shearing in the Paleoproterozoic Sefwi-Sunyani-Comoé region, West Africa. *Precambrian Research* 212-213: 155–168.

Jessell M, Santoul J, Baratoux L, Youbi N, Ernst RE, Metelka V, *et al.* 2015. An updated map of West African mafic dykes. *Journal of African Earth Sciences* 112: 440–450.

Kelsey DE, Powell R. 2011. Progress in linking accessory mineral growth and breakdown to major mineral evolution in metamorphic rocks: A thermodynamic approach in the Na_2O–CaO–K_2O–FeO–MgO–Al_2O_3–SiO_2–H_2O–TiO_2–ZrO_2 system. *Journal of Metamorphic Geology* 29: 151–166.

Kelsey DE, Clark C, Hand M. 2008. Thermobarometric modelling of zircon and monazite growth in melt-bearing systems: Examples using model metapelitic and metapsammitic granulites. *Journal of Metamorphic Geology* 26: 199–212.

Kirkland CL, Erickson TM, Johnson TE, Danišík M, Evans NJ, Bourdet J, *et al.* 2016. Discriminating prolonged, episodic or disturbed monazite age spectra: An example from the Kalak Nappe Complex, Arctic Norway. *Chemical Geology* 424: 96–110.

Koffi AY, Thébaud N, Kouamelan AN, Baratoux L, Bruguier O, Vanderhaeghe O, *et al.* 2022. Archean to Paleoproterozoic crustal evolution in the Sassandra-Cavally domain (Côte d'Ivoire, West Africa): Insights from Hf and U–Pb zircon analyses. *Precambrian Research* 382: 106875.

Kone J. 2020. Structure et métamorphisme de la ceinture Eburnéenne au Sénégal Oriental : signification en termes de contexte tectonique et de l'évolution thermomécanique de la croûte Eburnéenne. Université Toulouse 3 Paul Sabatier (UT3 Paul Sabatier), Université Cheikh Anta Diop de Dakar, 167 p.

Kone J, Vanderhaeghe O, Diatta F, Baratoux L, Thebaud N, Bruguier O, *et al.* 2020. Source and deposition age of the Dialé-Daléma metasedimentary series (Kédougou-Kéniéba Inlier, Senegal) constrained by U–Pb geochronology on detrital zircon grains. *Journal of African Earth Sciences* 165: 103801. https://doi.org/10.1016/j.jafrearsci.2020.103801.

Kouadio J-LH. 2017. Étude pétrostructurale des formations géologiques du Sud-Ouest de la Côte d'Ivoire (secteur Bliéron Grand-Béréby) : apport de la géochimie et du couple déformation-métamorphisme. Mémoire de thèse, Université Félix Houphouët-Boigny, UFR STRM, 276 p.

Kouamelan A-N. 1996. Géochronologie et geochimie des formations archeennes et proterozoïques de la Dorsale de Man en Côte d'Ivoire. Implications pour la transition Archéen-Protéozoïque. Thèse de doctorat, Université Rennes 1.

Kouamelan AN, Delor C, Peucat J-J. 1997. Geochronological evidence for reworking of Archean terrains during the Early Proterozoic (2.1 Ga) in the western Côte d'Ivoire (Man Rise-West African Craton). *Precambrian Research* 86: 177–199.

Kouamelan AN, Djro SC, Allialy ME, Paquette J-L, Peucat J-J. 2015. The oldest rock of Ivory Coast. *Journal of African Earth Sciences* 103: 65–70.

Kouamelan AN, Kra KSA, Djro SC, Paquette J-L, Peucat J-J. 2018. The Logoualé Band: A large Archean crustal block in the Kenema-Man domain (Man-Leo rise, West African Craton) remobilized during Eburnean orogeny (2.05 Ga). *Journal of African Earth Sciences* 148: 6–13.

Kranendonk MJV. 2010. Two types of Archean continental crust: Plume and plate tectonics on early Earth. *American Journal of Science* 310: 1187–1209.

Kroonenberg SB, Roever EWF de, Fraga LM, Reis NJ, Faraco T, Lafon J-M, *et al.* 2016. Paleoproterozoic evolution of the Guiana Shield in Suriname: A revised model. *Netherlands Journal of Geosciences*, Cambridge University Press 95: 491–522.

Krýza O, Závada P, Shu T, Semerád J. 2022. Modes and geometry of crustal-scale detachment folding in hot orogens – Insights from physical modeling. *Frontiers in Earth Science* 10.

Labou I, Benoit M, Baratoux L, Grégoire M, Ndiaye PM, Thebaud N, *et al.* 2020. Petrological and geochemical study of Birimian ultramafic rocks within the West African Craton: Insights from Mako (Senegal) and Loraboué (Burkina Faso) lherzolite/harzburgite/wehrlite associations. *Journal of African Earth Sciences* 162: 103677.

Ledru P, Pons J, Milesi JP, Feybesse JL, Johan V. 1991. Transcurrent tectonics and polycyclic evolution in the lower proterozoic of Senegal–Mali. *Precambrian Research* 50: 337–354.

Ledru P, Johan V, Milési JP, Tegyey M. 1994. Markers of the last stages of the Palaeoproterozoic collision: Evidence for a 2 Ga continent involving circum-South Atlantic provinces. *Precambrian Research*, Elsevier 69: 169–191.

Leite C de MM, Barbosa JSF, Goncalves P, Nicollet C, Sabaté P. 2009. Petrological evolution of silica-undersaturated sapphirine-bearing granulite in the Paleoproterozoic Salvador-Curaçá Belt, Bahia, Brazil. *Gondwana Research* 15: 49–70.

Lemoine S. 1988. Évolution géologique de la région de Dabakala (NE de la Côte d'Ivoire) au Protérozoïque inférieur : possibilités d'extension au reste de la Côte d'Ivoire et au Burkina Faso. Thèse d'État, Université de Clermont-Ferrand, 388 p.

Lemoine S, Tempier P, Bassot JP, Caen-Vachette M, Vialette Y, Wenmenga U, *et al.* 1985. The Burkinian, an orogenic cycle, precursor of the Eburnean of West Africa. *Coll. Afr. Geol. 13th* 27.

Leube A, Hirdes W, Mauer R, Kesse GO. 1990. The early Proterozoic Birimian Supergroup of Ghana and some aspects of its associated gold mineralization. *Precambrian Research* 46: 139–165.

Liégeois J-P, Benhallou A, Azzouni-Sekkal A, Yahiaoui R, Bonin B. 2005. The Hoggar swell and volcanism: Reactivation of the Precambrian Tuareg Shield during Alpine convergence and West

African Cenozoic volcanism. In: *Plates, plumes and paradigms*. Geological Society of America, Vol. 388.

Lin S, Jiang D, Williams PF. 1998. Transpression (or transtension) zones of triclinic symmetry: Natural example and theoretical modelling. *Geological Society, London, Special Publications*, The Geological Society of London 135: 41–57.

Lompo M. 2009. Geodynamic evolution of the 2.25–2.0 Ga Palaeoproterozoic magmatic rocks in the Man-Leo Shield of the West African Craton. A model of subsidence of an oceanic plateau. *Geological Society, London, Special Publications*. The Geological Society of London 323: 231–254.

Lompo M. 2010. Paleoproterozoic structural evolution of the Man-Leo Shield (West Africa). Key structures for vertical to transcurrent tectonics. *Journal of African Earth Sciences* 58: 19–36.

Louis-Napoléon A, Gerbault M, Bonometti T, Thieulot C, Martin R, Vanderhaeghe O. 2020. 3-D numerical modelling of crustal polydiapirs with volume-of-fluid methods. *Geophysical Journal International* 222: 474–506.

Louis-Napoléon A, Gerbault M, Bonometti T, Vanderhaeghe O, Martin R. 2021. Modeling gravitational instabilities in the partially molten crust with a Volume-Of-Fluid method. In: *Paper presented at the EGU General Assembly Conference Abstracts EGU21-5892*.

Ludwig KR. 2003. User's manual for a geochronological toolkit for Microsoft Excel (Isoplot/Ex version 3.0). *Berkeley Geochronology Center, Special Publication* 4: 1–71.

Machado N, Noce CM, Ladeira EA, De Oliveira OB. 1992. U–Pb geochronology of Archean magmatism and Proterozoic metamorphism in the Quadrilátero Ferrífero, southern São Francisco Craton, Brazil. *GSA Bulletin* 104: 1221–1227.

Mahar EM, Baker JM, Powell R, Holland TJB, Howell N. 1997. The effect of Mn on mineral stability in metapelites. *Journal of Metamorphic Geology* 15: 223–238.

Martin H. 1994. Chapter 6: The Archean grey gneisses and the genesis of continental crust. In: Condie KC, ed. *Developments in Precambrian Geology*. Elsevier, pp. 205–259.

Maruyama S, Santosh M, Azuma S. 2018. Initiation of plate tectonics in the Hadean: Eclogitization triggered by the ABEL Bombardment. *Geoscience Frontiers* 9: 1033–1048.

McFarlane H. 2018. The geodynamic and tectonic evolution of the Palaeoproterozoic Sefwi Greenstone Belt, West African Craton (Ghana). PhD Thesis, Université Toulouse 3 Paul Sabatier (UT3 Paul Sabatier), Monash University (Australie).

McFarlane CRM, Connelly JN, Carlson WD. 2006. Contrasting response of monazite and zircon to a high-T thermal overprint. *Lithos* 88: 135–149.

McFarlane HB, Ailleres L, Betts P, Ganne J, Baratoux L, Jessell MW, *et al.* 2019. Episodic collisional orogenesis and lower crust exhumation during the Palaeoproterozoic Eburnean Orogeny: Evidence from the Sefwi Greenstone Belt, West African Craton. *Precambrian Research* 325: 88–110.

Medeiros Júnior EB, Degler R, Jordt-Evangelista H, Queiroga GN, Schulz B, Marques RA. 2016. Electron microprobe Th–U–Pb monazite dating and metamorphic evolution of the Acaiaca Granulite Complex, Minas Gerais, Brazil. *Rem: Revista Escola de Minas* 69: 21–32.

Milési J-P, Heinry C, Sylvain J-P. 1989. Minéralisations aurifères de l'Afrique de l'ouest leurs relations avec l'évolution lithostructurale au Proterozoique inférieur. *Bureau de recherches géologiques et minières* 497: 3–98.

Milési J-P, Ledru P, Feybesse J-L, Dommanget A, Marcoux E. 1992. Early proterozoic ore deposits and tectonics of the Birimian orogenic belt, West Africa. *Precambrian Research* 58: 305–344.

Miyashiro A. 1961. Evolution of metamorphic belts. *Journal of Petrology* 2: 277–311.

Montel J-M, Foret S, Veschambre M, Nicollet C, Provost A. 1996. Electron microprobe dating of monazite. *Chemical Geology* 131: 37–53.

Ndiaye PM, Robineau B, Moreau C. 1989. Deformation et metamorphisme des formations birrimiennes en relation avec la mise en place du granite eburneen de Saraya (Sénégal Oriental). *Bulletin de la Société Géologique de France* V: 619–625.

Noce CM, Machado N, Teixeira W. 1998. U–Pb geochronology of gneisses and granitoids in the Quadrilátero Ferrífero (southern São Francisco Craton): Age constraints for Archean and Paleoproterozoic magmatism and metamorphism. *Revista Brasileira de Geociências* 28: 95–102.

Nomade S, Chen Y, Pouclet A, Féraud G, Théveniaut H, Daouda BY, *et al.* 2003. The Guiana and the West African Shield Palaeoproterozoic grouping: New palaeomagnetic data for French Guiana and the Ivory Coast. *Geophysical Journal International* 154: 677–694.

Onstott TC, Hargraves RB. 1981. Proterozoic transcurrent tectonics: Palaeomagnetic evidence from Venezuela and Africa. *Nature*, Nature Publishing Group 289: 131–136.

Opare-Addo E, Browning P, John BE. 1993. Pressure-temperature constraints on the evolution of an Early proterozoic plutonic suite in southern Ghana, West Africa. *Journal of African Earth Sciences (and the Middle East)* 17: 13–22.

Palin RM, Santosh M, Cao W, Li S-S, Hernández-Uribe D, Parsons A. 2020. Secular metamorphic change and the onset of plate tectonics. *Earth-Science Reviews* 207: 103172.

Papon A. 1973. Géologie et minéralisations du Sud-Ouest de la Côte d'Ivoire : synthèse des travaux de l'opération SASCA.

Parra-Avila LA, Kemp AIS, Fiorentini ML, Belousova E, Baratoux L, Block S, *et al.* 2017. The geochronological evolution of the Paleoproterozoic Baoulé-Mossi domain of the southern West African Craton. *Precambrian Research* 300: 1–27. https://doi.org/10.1016/j.precamres.2017.07.036.

Peucat J-J, Capdevila R, Drareni A, Mahdjoub Y, Kahoui M. 2005. The Eglab massif in the West African Craton (Algeria), an original segment of the Eburnean orogenic belt: Petrology, geochemistry and geochronology. *Precambrian Research* 136: 309–352.

Peucat J-J, Figueiredo Barbosa JS, Conceição de Araújo Pinho I, Paquette J-L, Martin H, Fanning CM, *et al.* 2011. Geochronology of granulites from the south Itabuna-Salvador-Curaçá Block, São Francisco Craton (Brazil): Nd isotopes and U–Pb zircon ages. *Journal of South American Earth Sciences* 31: 397–413.

Pitra P, Kouamelan AN, Ballevre M, Peucat J-J. 2010a. Palaeoproterozoic high-pressure granulite overprint of the Archean continental crust: Evidence for homogeneous crustal thickening (Man Rise, Ivory Coast). *Journal of Metamorphic Geology*, Wiley Online Library 28: 41–58.

Poitrasson F, Chenery S, Shepherd TJ. 2000. Electron microprobe and LA-ICP-MS study of monazite hydrothermal alteration: Implications for U–Th–Pb geochronology and nuclear ceramics. *Geochimica et Cosmochimica Acta* 64: 3283–3297.

Pons J, Barbey P, Dupuis D, Léger JM. 1995. Mechanisms of pluton emplacement and structural evolution of a 2.1 Ga juvenile continental crust: The Birimian of southwestern Niger. *Precambrian Research*, Elsevier 70: 281–301.

Potrel A, Peucat JJ, Fanning CM, Auvray B, Burg JP, Caruba C. 1996. 3.5 Ga old terranes in the West African Craton, Mauritania. *Journal of the Geological Society*, The Geological Society of London 153: 507–510.

Pouclet A, Vidal M, Delor C, Simeon Y, Alric G. 1996. Le volcanisme birimien du nord-est de la Côte-d'Ivoire, mise en evidence de deux phases volcano-tectoniques distinctes dans l'evolution geodynamique du Paleoproterozoique. *Bulletin de la Société géologique de France*, Société Géologique de France 167: 529–541.

Pouclet A, Doumbia S, Vidal M. 2006. Geodynamic setting of the Birimian volcanism in central Ivory Coast (western Africa) and its place in the Palaeoproterozoic evolution of the Man Shield. *Bulletin de la Société Géologique de France*, GeoScienceWorld 177: 105–121.

Rey PF, Houseman G. 2006. Lithospheric scale gravitational flow: The impact of body forces on orogenic processes from Archaean to Phanerozoic. *Geological Society, London, Special Publications*, The Geological Society of London 253: 153–167.

Rollinson H. 2016. Archaean crustal evolution in West Africa: A new synthesis of the Archaean geology in Sierra Leone, Liberia, Guinea and Ivory Coast. *Precambrian Research* 281: 1–12.

Rollinson HR, Cliff RA. 1982. New Rb–Sr age determinations on the Archaean basement of Eastern Sierra Leone. *Precambrian Research* 17: 63–72.

Rubatto D, Williams IS, Buick IS. 2001. Zircon and monazite response to prograde metamorphism in the Reynolds Range, Central Australia. *Contributions to Mineralogy and Petrology* 140: 458–468.

Schmidt C, Rickers K, Bilderback DH, Huang R. 2007. *In situ* synchrotron-radiation XRF study of REE phosphate dissolution in aqueous fluids to 800 °C. *Lithos* 95: 87–102.

Schrank A, Machado N. 1996. Idades U–Pb em monazitas e zircões das minas de Morro Velho e Passagem de Mariana-Quadrilátero Ferrífero (MG). *SBG, Cong. Bras. Geol* 39: 470–472.

Schulmann K, Lexa O, Štípská P, Racek M, Tajčmanová L, Konopásek J,*et al.* 2008. Vertical extrusion and horizontal channel flow of orogenic lower crust: Key exhumation mechanisms in large hot orogens? *Journal of Metamorphic Geology* 26: 273–297.

Seydoux-Guillaume A-M, Montel J-M, Bingen B, Bosse V, de Parseval P, Paquette J-L, *et al.* 2012. Low-temperature alteration of monazite: Fluid mediated coupled dissolution-precipitation, irradiation damage, and disturbance of the U–Pb and Th–Pb chronometers. *Chemical Geology* 330-331: 140–158.

Silva LJHD-R, Oliveira JG de, Gaál EG. 1996. Implication of the caraíba deposit's structural controls on the emplacement of the cu-bearing hypersthenites of the Curaçá Valley, Bahia Brazil. Universidade Federal do Paraná – Pró-Reitoria de pesquisa e pós-graduação.

Stern RJ. 2005. Evidence from ophiolites, blueschists, and ultrahigh-pressure metamorphic terranes that the modern episode of subduction tectonics began in Neoproterozoic time. *Geology* 33: 557–560.

Štípská P, Chopin F, Skrzypek E, Schulmann K, Pitra P, Lexa O, *et al.* 2012. The juxtaposition of eclogite and mid-crustal rocks in the Orlica-Śnieżnik Dome, Bohemian Massif. *Journal of Metamorphic Geology* 30: 213–234.

Tagini B. 1971. Esquisse structurale de la Côte d'Ivoire. Essai de géotectonique régionale. Thèse Université de Lausanne, Société d'État pour le Développement minière de la Côte d'Ivoire.

Teufel S, Heinrich W. 1997. Partial resetting of the U–Pb isotope system in monazite through hydrothermal experiments: An SEM and U–Pb isotope study. *Chemical Geology* 137: 273–281.

Thiéblemont D. 2016. An updated geological map of Africa at 1/10 000 000 scale. In: *Paper presented at the 35th International Geological Congress: IGC 2016*.

Thiéblemont D, Delor C, Cocherie A, Lafon JM, Goujou JC, Baldé A, *et al.* 2001. A 3.5 Ga granite–gneiss basement in Guinea: Further evidence for early archean accretion within the West African Craton. *Precambrian Research* 108: 179–194.

Thiéblemont D, Goujou JC, Egal E, Cocherie A, Delor C, Lafon JM, *et al.* 2004. Archean evolution of the Leo Rise and its Eburnean reworking. *Journal of African Earth Sciences* 39: 97–104.

Traoré K, Chardon D, Naba S, Wane O, Bouaré ML. 2022. Paleoproterozoic collision tectonics in West Africa: Insights into the geodynamics of continental growth. *Precambrian Research* 376: 106692.

Triboulet C, Feybesse J-L. 1998. Les métabasites birimiennes et archéennes de la région de Toulepleu-Ity (Côte-d'Ivoire) : des roches portées à 8 kbar (≈ 24 km) et 14 kbar (≈ 42 km) au Paléoprotérozoïque. *Comptes Rendus de l'Académie des Sciences – Series IIA – Earth and Planetary Science* 327: 61–66.

Van Achterbergh E, Ryan CG, Jackson SE, Griffin WL. 2001. Data reduction software for LA-ICP-MS: Appendix. In: Sylvester PJ, ed. *Laser Ablation-ICP Mass Spectrometry in the Earth Sciences: Principles and applications*, pp. 239–243.

Vanderhaeghe O. 2009. Migmatites, granites and orogeny: Flow modes of partially-molten rocks and magmas associated with melt/solid segregation in orogenic belts. *Tectonophysics* 477: 119–134.

Vanderhaeghe O. 2012. The thermal-mechanical evolution of crustal orogenic belts at convergent plate boundaries: A reappraisal of the orogenic cycle. *Journal of Geodynamics* 56-57: 124–145.

Vanderhaeghe O, Teyssier C. 2001. Partial melting and flow of orogens. *Tectonophysics, Partial Melting of Crust and Flow of Orogens* 342: 451–472. https://doi.org/10.1016/S0040-1951(01)00175-5.

Vanderhaeghe O, Ledru P, Thiéblemont D, Egal E, Cocherie A, Tegyey M, *et al.* 1998. Contrasting mechanism of crustal growth: Geodynamic evolution of the Paleoproterozoic granite-greenstone belts of French Guiana. *Precambrian Research* 92: 165–193.

Vanderhaeghe O, Kruckenberg SC, Gerbault M, Martin L, Duchêne S, Deloule E. 2018. Crustal-scale convection and diapiric upwelling of a partially molten orogenic root (Naxos dome, Greece). *Tectonophysics* 746: 459–469.

Vanderhaeghe O, Guergouz C, Fabre C, Duchêne S, Baratoux D. 2019. Secular cooling and crystallization of partially molten Archaean continental crust over 1 Ga. *Comptes Rendus Geoscience* 351: 562–573.

Vanderhaeghe O, Laurent O, Gardien V, Moyen J-F, Gébelin A, Chelle-Michou C, *et al.* 2020. Flow of partially molten crust controlling construction, growth and collapse of the Variscan orogenic belt: The geologic record of the French Massif Central. *Bulletin de la Société Géologique de France* 191: 25. https://doi.org/10.1051/bsgf/2020013.

Vidal M, Delor C, Pouclet A, Simeon Y, Alric G. 1996. Geodynamic evolution of the West Africa between 2.2 and 2 Ga: The Archaean style of the Birimian greenstone belts and the sedimentary basins in northeastern Ivory Coast. *Bulletin de la Societe Geologique de France* 167: 307–319.

Vidal M, Gumiaux C, Cagnard F, Pouclet A, Ouattara G, Pichon M. 2009. Evolution of a Paleoproterozoic "weak type" orogeny in the West African Craton (Ivory Coast). *Tectonophysics* 477: 145–159.

Vlach SRF, Neto MC, Caby R, Basei MAS. 2003. Contact metamorphism in metapelites from the Nova Lima group, Rio Das Velhas Supergroup, Quadrila. Tero ferrifero: A monazite Th–U–Pbt dating by the electron-probe microanalyser. In: *IV South American Symposium on Isotope Geology, Salvador. Short Papers*, pp. 307–310.

Wane O, Liégeois J-P, Thébaud N, Miller J, Metelka V, Jessell M. 2018. The onset of the Eburnean collision with the Kenema-Man Craton evidenced by plutonic and volcano sedimentary rock record of the Masssigui region, southern Mali. *Precambrian Research* 305: 444–478.

WAXI report, AMIRA Global. 2018. West African Exploration Initiative Stage 3. Australia: AMIRA International Limited, 925 p.

White RW, Powell R. 2002. Melt loss and the preservation of granulite facies mineral assemblages. *Journal of Metamorphic Geology* 20: 621–632.

White RW, Powell R, Holland TJB, Worley BA. 2000. The effect of TiO_2 and Fe_2O_3 on metapelitic assemblages at greenschist and amphibolite facies conditions: Mineral equilibria calculations in the system K_2O–FeO–MgO–Al_2O_3–SiO_2–H_2O–TiO_2–Fe_2O_3. *Journal of Metamorphic Geology* 18: 497–511.

White RW, Powell R, Holland TJB. 2007. Progress relating to calculation of partial melting equilibria for metapelites. *Journal of Metamorphic Geology* 25: 511–527.

White A, Burgess R, Charnley N, Selby D, Whitehouse M, Robb L, *et al.* 2014. Constraints on the timing of late-Eburnean metamorphism, gold mineralisation and regional exhumation at Damang mine, Ghana. *Precambrian Research* 243: 18–38.

Williams HR. 1988. The archaean kasila group of Western Sierra Leone: Geology and relations with adjacent granite-greenstone terrane. *Precambrian Research* 38: 201–213.

Williams ML, Jercinovic MJ, Harlov DE, Budzyń B, Hetherington CJ. 2011. Resetting monazite ages during fluid-related alteration. *Chemical Geology* 283: 218–225.

Yakymchuk C, Brown M. 2014. Behaviour of zircon and monazite during crustal melting. *Journal of the Geological Society* 171: 465–479.

Cite this article as: Koffi AY, Baratoux L, Pitra P, Kouamelan AN, Vanderhaeghe O, Thébaud N, Bruguier O, Block S, Fossou Kouadio HJ-L, Kone J. 2023. A tectonic model for the juxtaposition of granulite- and amphibolite-facies rocks in the Eburnean orogenic belt (Sassandra-Cavally domain, Côte d'Ivoire), *BSGF - Earth Sciences Bulletin* 194: 11.